Ge and Si isotope behavior during intense tropical weathering

J. Jotautas Baronas[1,2], A. Joshua West[1], Kevin W. Burton[3], Douglas E. Hammond[1], Sophie Opfergelt[4], Philip A.E. Pogge von Strandmann[5], Rachael H. James[6], Olivier J. Rouxel[7]

[1]Department of Earth Sciences, University of Southern California, Los Angeles, CA 90089, USA
[2]Department of Earth Sciences, University of Cambridge, Cambridge CB2 3EQ, UK
[3]Department of Earth Sciences, Durham University, Durham DH1 3LE, UK
[4]Earth and Life Institute, Université catholique de Louvain, Croix du Sud bte L7.05.10, 1348 Louvain-la-Neuve, Belgium
[5]London Geochemistry and Isotope Centre (LOGIC), Institute of Earth and Planetary Sciences, University College London and Birkbeck, University of London, Gower Street, London WC1E 6BT, UK
[6]School of Ocean and Earth Science, National Oceanography Centre Southampton, University of Southampton Waterfront Campus, Southampton SO14 3ZH, UK
[7]IFREMER, Centre de Brest, Unité Géosciences Marines, 29280 Plouzané, France

Key Points:

- Very low Ge and Si isotope ratios in clays and bulk soils, reflecting intense chemical weathering.
- Si cycling is strongly influenced by vegetation in extremely weathered soils.
- In global volcanic soils, Si isotopes and Ge/Si reflect Si loss, while Ge isotopes reflect Ge loss.

Corresponding author: J. Jotautas Baronas, jotautas.baronas@gmail.com

Abstract

Chemical weathering of volcanic rocks in warm and humid climates contributes disproportionately to global solute fluxes. Geochemical signatures of solutes and solids formed during this process can help quantify and reconstruct volcanic weathering in the past. Here, we measured silicon (Si) and germanium (Ge) isotope ratios of the soils, clays, and fluids of a tropical lowland rainforest in Costa Rica. The bulk topsoil is intensely weathered and isotopically light (mean±1σ: δ^{30}Si = –2.1 ± 0.3‰, δ^{74}Ge = –0.13 ± 0.12‰) compared to the parent bedrock (δ^{30}Si = –0.11 ± 0.05‰, δ^{74}Ge = 0.59 ± 0.07‰). Neoforming clays are even lighter (δ^{30}Si = –2.5 ± 0.2‰, δ^{74}Ge = –0.16 ± 0.09‰), demonstrating a whole-system isotopic shift in extremely weathered systems. The lowland streams represent mixing of dilute local fluids (δ^{30}Si = 0.2 – 0.6‰, δ^{74}Ge = 2.2 – 2.6‰) with solute-rich interbasin groundwater (δ^{30}Si = 1.0 ± 0.2‰, δ^{74}Ge = 4.0‰). Using a Ge-Si isotope mass balance model, we calculate that 91 ± 9% of Ge released via weathering of lowland soils is sequestered by neoforming clays, 9 ± 9% by vegetation, and only 0.2 ± 0.2% remains dissolved. In contrast, vegetation plays an important role in the Si cycle, sequestering 39 ± 14% of released Si. Globally, volcanic soil δ^{74}Ge closely tracks the depletion of Ge by chemical weathering (τ_{Ge}), whereas δ^{30}Si and Ge/Si both reflect the loss of Si (τ_{Si}). Because of the different chemical mobilities of Ge and Si, a δ^{74}Ge-δ^{30}Si multi-proxy system is sensitive to a wider range of weathering intensities than each isotopic system in isolation.

1 Introduction

Physical and chemical interaction of water with rocks shapes the land surface, supplies dissolved nutrients and trace elements to terrestrial and marine ecosystems, and modulates climate via the consumption of atmospheric CO_2 (e.g., Frings & Buss, 2019). The latter process, which relies on the chemical weathering of silicate rocks, has been proposed as a major mechanism stabilizing (Walker et al., 1981; Berner et al., 1983) or perturbing (Raymo & Ruddiman, 1992; Macdonald et al., 2019) climate at different stages of Earth history. A true test of these hypotheses therefore requires the reconstruction of silicate weathering over geological timescales. Although there are currently no methods that can reliably reconstruct the absolute chemical weathering fluxes in the past, the relative intensity of chemical weathering is to some degree reflected in records of ocean chemistry (e.g., Froelich et al., 1992; Hathorne & James, 2006; Misra & Froelich, 2012; Li & Elderfield, 2013) and in the geochemical signatures of secondary weathering phases formed in soils (e.g., Amundson, 2013; Bouchez et al., 2013). A robust understanding of how elemental and isotopic proxy signatures are generated in the weathering environment is needed to interpret geological sedimentary records.

The chemical weathering of silicate rocks releases constituent elements to solution, with variable fractions of each element retained in secondary weathering phases, such as aluminosilicate clays and refractory oxides. The formation of such phases often results in the fractionation of element ratios due to differing stoichiometry and thermodynamic properties of the dissolving and precipitating phases and in the fractionation of isotope ratios due to kinetic (e.g., Watkins et al., 2017) and quantum vibrational effects (e.g., Blanchard et al., 2017). With limited erosion and continued chemical weathering (e.g., in humid tropical environments), as primary phases are depleted, secondary phases can then become thermodynamically destabilized, resulting in further chemical and isotopic fractionation. Over thousand-year and longer timescales, this fractionation results in preferential loss of certain elements and isotopes from the critical zone, with the remaining solids containing a record of the long-term weathering intensity.

Different silicate weathering intensity proxies have been investigated, most notably germanium to silicon (Ge/Si) ratios (Murnane & Stallard, 1990; Froelich et al., 1992), lithium isotope ratios (e.g., Hathorne & James, 2006; Misra & Froelich, 2012; Dellinger et al., 2015; Pogge von Strandmann & Henderson, 2015), and silicon isotope ratios (e.g., Ziegler et al., 2005; Georg et al., 2006a; Frings et al., 2016) in both the dissolved and the solid products of weathering. Recently, germanium isotopes have also been shown to trace chemical weathering of silicates

(Baronas et al., 2017, 2018). However, each elemental or isotopic proxy reflects a multitude of processes in the critical zone, and – if reconstructions are based on marine records – in the ocean, resulting in a range of possible interpretations of each proxy record (e.g., Hammond et al., 2004; Li & West, 2014; Frings et al., 2016; Baronas et al., 2017).

Germanium is a trace element that is chemically similar to Si, and in the critical zone, both elements are primarily sourced from silicate rocks that exhibit Ge/Si ratios in the range of 1-3 μmol/mol (De Argollo & Schilling, 1978; Bernstein, 1985; Mortlock & Froelich, 1987). During the precipitation of secondary weathering phases, dissolved Ge is removed from solution preferentially over dissolved Si, resulting in natural waters with Ge/Si ratios of 0.1-3 μmol/mol (Froelich et al., 1985; Mortlock & Froelich, 1987; Murnane & Stallard, 1990; Froelich et al., 1992; Kurtz et al., 2002; Anders et al., 2003; Lugolobi et al., 2010; Meek et al., 2016; Baronas et al., 2017, 2018). Similarly, Si isotope ratios (δ^{30}Si) are fractionated during the formation of secondary weathering solids which preferentially incorporate lighter Si isotopes (δ^{30}Si = –3 to 0‰), leaving the corresponding soil waters and streams isotopically heavy (δ^{30}Si = 0 to 3‰) relative to primary silicates (δ^{30}Si ≈ –0.3 to 0 ‰) (e.g., Ziegler et al., 2005; Georg et al., 2007; Opfergelt & Delmelle, 2012; Frings et al., 2016). In addition, terrestrial vegetation can incorporate significant amounts of soil water Si (primarily in amorphous silica phytoliths), again preferentially removing light isotopes (e.g., Ding et al., 2005; Opfergelt et al., 2006; Opfergelt & Delmelle, 2012). In contrast, most plants discriminate against Ge, and as a result the phytoliths exhibit low Ge/Si values (Derry et al., 2005; Blecker et al., 2007; Lugolobi et al., 2010; Sparks et al., 2010; Meek et al., 2016). The combined use of δ^{30}Si and Ge/Si therefore allows evaluation of the vegetation influence on the local Si cycle, both on the soil profile scale (Cornelis et al., 2010; Opfergelt et al., 2010; White et al., 2012; Cornelis et al., 2014) and on the catchment scale (Baronas et al., 2018).

Two recent studies have shown that Ge isotopes behave similarly to Si during weathering, with fluids enriched (δ^{74}Ge = 0.9 to 5.5‰; Baronas et al. (2018)) and weathered solids depleted in heavy isotopes (δ^{74}Ge = –0.1 to 0.6‰; Qi et al. (2019)) relative to primary igneous silicates (δ^{74}Ge = 0.4 to 0.8‰; Rouxel and Luais (2017)). Over geological timescales, the heavy isotopic signatures of the fluids can only be maintained if the secondary solids are continuously eroded from the continents (Bouchez et al., 2013). In contrast, continued chemical weathering of soils in erosionally-limited regimes results in progressive depletion of ^{30}Si, driving all soil materials and weathering fluids towards lower δ^{30}Si (Ziegler et al., 2005; Opfergelt et al., 2012). There are currently, however, very few detailed systematic studies of Si (and even more so Ge) isotope behavior in such extremely chemically weathered environments.

In this study, we have investigated Ge/Si, δ^{30}Si, and δ^{74}Ge distributions in the ground waters, streams, and deeply weathered volcanic soils of a tropical rainforest in Costa Rica, to better understand how these proxies reflect intense tropical chemical weathering and other critical zone processes locally and globally.

2 Methods

2.1 Site description

The study site spans the La Selva Biological Station of the Organization for Tropical Studies (OTS) in the Atlantic lowlands of Costa Rica (Fig 1). The elevation ranges from 20 to 140 m above sea level. The study site lies 35 km northeast of Barva Volcano. Rainfall averages 4 m/y and is relatively constant in spring through fall (300-500 mm/month), with a minimum of 150-160 mm in January-February (Genereux & Jordan, 2006). The mean annual temperature is 24-26 °C and is relatively constant all year round (Sanford et al., 1994). The warm and wet climate supports a tropical wet forest ecosystem.

The bedrock primarily consists of several >1.2 My old andesitic plagioclase-rich lava flows (Alvarado Induni, 1990; McDade et al., 1994). The study area is underlain by >20 m thick, strongly weathered soils, developed on top of the lava flows, as well as alluvial Holocene-

Pleistocene deposits at the lowest elevations along the Rio Sarapiqui and Rio Puerto Viejo rivers. The mineralogy of bulk soils has been described in detail previously by Kleber et al. (2007). Briefly, the soils are classified as Oxisols and are primarily composed of gibbsite, and various forms of halloysite-kaolinite, with smaller amounts of goethite and hematite. Trace amounts of quartz and magnetite are also present.

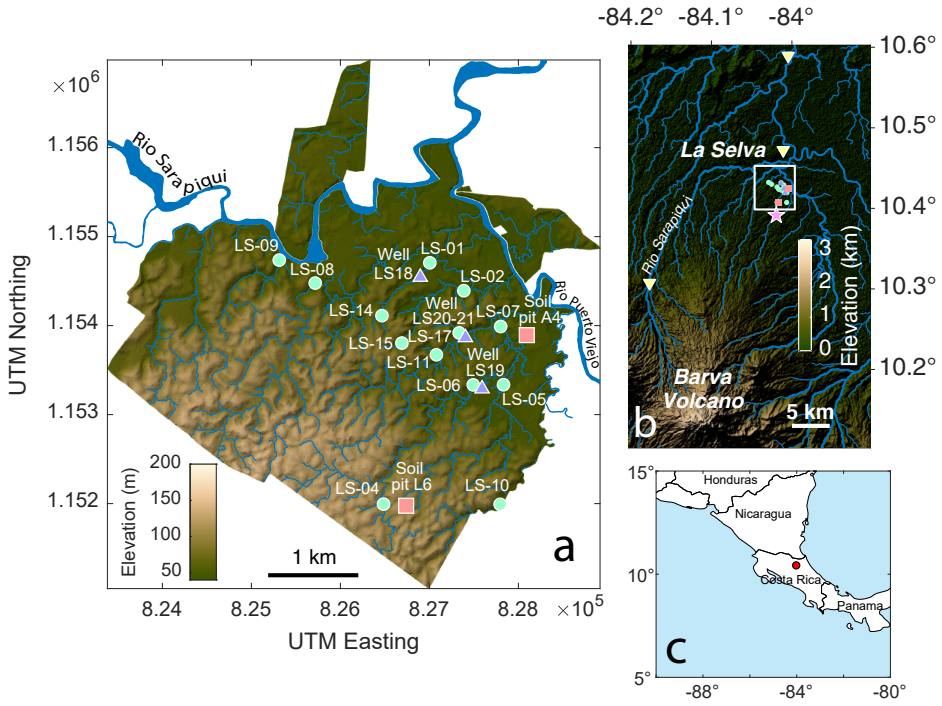

Figure 1. Map of the study site, showing sample locations in the La Selva Biological Station (a), the regional setting, including the nearby Barva Volcano (b), and the setting within Central America (c). Stream samples locations are shown as cyan circles, sampled wells as purple triangles, and soil pits as red squares. In panel (b), the interbasin groundwater sample (CR5) that was collected at the Guacimo spring is shown as a pink star and the samples of the large Sarapiqui river are shown as yellow triangles.

2.2 Sample collection

Samples were collected from the La Selva Biological Station and neighboring areas between 14th and 20th May 2010. Most samples were collected from streams within the Biological Station, accessed by foot using the station trail network. Additional samples (prefix CR) were collected from rivers draining the wider region, accessed by road. Guacimo Spring, discharging about 1 km southwest of the study area, was also sampled, as it reflects the composition of volcanic interbasin groundwater, recharged at higher elevations on the slopes of Barva Volcano (e.g., Pringle et al., 1990; Genereux et al., 2009).

Stream and river water samples were collected in pre-rinsed 15 L collapsible plastic containers and transported directly back to the laboratory at the La Selva Biological Station. Ground waters were collected from existing shallow (<1 m deep) wells at La Selva (Genereux et al., 2005) using a plastic bailer. Temperature, pH, and conductivity were measured in situ using a handheld meter, with pH calibrated daily using pH buffers. All water samples were immediately (typically within 1 hour) filtered through 142 mm diameter, 0.2 μm polyethersulfone (PES) membrane filters using a peristaltic pump and an inline Sartorious PFA filter holder. The

filtration apparatus was cleaned between each sample and pre-rinsed with sample before collecting filtrate. For the analyses reported in this study, three aliquots of filtrate were collected into separate low density polyethylene (LDPE) bottles. One bottle was filled completely and left unpreserved, for analysis of anion concentrations. The other bottle was acidified with quartz-distilled HNO_3 to pH < 2, for cation, Ge concentration, and Si isotope ratio analyses conducted in this study. A third larger 500-1000 mL aliquot was also acidified and later used for Ge isotope analysis. Alkalinity was measured using Gran titration on a separate unfiltered water aliquot.

Filter papers were stored in plastic bags and returned to the University of Oxford, where suspended sediment was removed with a spatula and dried at 60 °C. A small amount of fine-grained material could not be removed from the filter papers, but this small proportion is not expected to bias analysis of sediment composition. Sediment from the stream bed was collected at selected sites in plastic bags and dried at 60 °C (referred to as "bedload" samples). Since bedrock exposures are not present at La Selva or in the immediately surrounding area, visibly well-preserved clasts of rock were collected from selected stream sites to provide a sampling of rock from the region.

Soils were collected from two soil pits (originally 3-4m depth) dug in 1997 at the La Selva "Carbono" plots (Clark & Clark, 2000; Veldkamp et al., 2003; Kleber et al., 2007). Soil pit IDs were adopted from the previous plot naming conventions, with samples collected from the same two pits (A4 and L6) that were studied in detail for mineralogical composition by Kleber et al. (2007). Pit A4 reflects "old alluvial" soil developed on a river terrace probably of Pleistocene age, while L6 is "residual" soil developed on ~1.2 Ma lava flows (Veldkamp et al., 2003). Both are deeply weathered Oxisols, with similar parent material but differing in age (Kleber et al., 2007). Soils were collected from the exposed pit walls. Since some additional weathering had occurred since the pits were dug, ~50 cm was excavated into the side of the pit wall before collecting samples into plastic bags with a hand trowel. Clay fractions (operationally defined as the <2 μm particle size fraction) were separated from selected solid samples (including soils and stream bed sediment) by settling in deionized water after sonication and dispersion by addition of a sodium phosphate salt.

To collect soil pore waters, rhizon samplers (10 cm length, 2.0 mm diameter, 0.15 μm pore-size PES) were inserted horizontally into the excavated surface. Syringes were left to fill for ~24 hours before dispensing the collected pore waters into pre-washed 30 mL PP bottles. Vegetation samples were collected from understory vegetation, selecting a single individual from species that appeared to be visibly common in the area around each soil pit. Species were not identified. Samples of mature leaves were cut and collected in a plastic bag, transported to the laboratory, cleaned, and dried before grinding and ashing for analysis. All water, sediment, and soil samples were refrigerated following collection, except during the air transport (~24 hours) from Costa Rica to Oxford.

2.3 Major and trace element analyses

Solid samples were powdered using a mortar and pestle and dissolved in a HF/HNO_3 mixture in Teflon vials at elevated temperature. Solutions were evaporated to dryness, and residual salts dissolved in 2% HNO_3 for analysis by ICP-MS (Thermo Scientific X-Series II) at the University of Southampton. Measurements were calibrated against four certified rock reference materials (JGb-1, JB-1a, JA-2, MAG-1) and the reproducibility of the analyses was better than ±5% for major elements and better than ±3% for trace elements. Measured concentrations were within ±5% of the certified or recommended values for all elements except K (±10%). Si concentrations in solids were measured after NaOH fusion, as described below. Si measurement accuracy of solids was ±10%, as confirmed by analyses of three certified rock reference materials (BIR-1, DTS-1, SCO-1).

The untreated aliquot of each water sample was analyzed for major anions (Cl^-, SO_4^{2-}, and NO_3^-) by Ion Chromatography at the University of Southern California using a Metrohm IC 861 equipped with an A4/150 anion exchange column with conductivity suppression, us-

ing a 3.2 mM Na_2CO_3 / 1.0 mM $NaHCO_3$ eluent with a flow rate of 0.7 mL/min. Conductivity signals were calibrated against a series of standards prior to the analytical session. A certified reference material (ION-915, Environment Canada) was run after every 10-15 samples. All analyses were within the range of certified values, and replicate analyses were within 10% (2 σ).

Other major and trace elements, including Ca, Mg, Na, K, Sr, Li, and U, were measured on the acidified portion of each water sample using a Thermo Element2 ICP-MS (inductively coupled plasma mass spectrometer) at the University of Oxford. All elements were analyzed in low resolution mode. Intensities for trace elements were calibrated using multiple dilutions of an in-house standard solution with a composition similar to average river water. Major elements were calibrated using dilutions of the TROIS-94 certified reference water (Trois Rivers, Environment Canada). Indium was used as an internal standard to correct for signal drift during the analytical session. Charge balance was within 20% for all but one sample (LS06), and was within 5% for most samples. Dissolved Si concentrations were measured by spectrophotometry using the molybdate blue method with citric and amino acid reagents.

2.4 Germanium concentration analysis

Dissolved Ge concentrations in water samples were measured using isotope-dilution-hydride-generation-ICP-MS based on the method by Mortlock and Froelich (1996), as modified by Baronas et al. (2016). Briefly, a mono-isotopic ^{70}Ge spike was added to 5 mL of sample gravimetrically, and the sample diluted to 20 mL with 0.01 M distilled HCl. Dissolved Ge was converted to hydride by reacting with $NaBH_4$ and the resulting GeH_4 gas pre-concentrated on a liquid N_2 trap prior to being injected into a Thermo Element 2 ICP-MS instrument at the University of Southern California. Ge concentrations in solid samples were determined using MC-ICP-MS, after double spiking, digestion, and chromatographic separation for $\delta^{74}Ge$ analysis, as described below. Ge concentration in each sample was determined based on the measured $^{70}Ge/^{74}Ge$ ratio.

2.5 Silicon isotope analysis

Fusion of solids. Solid samples were digested using a fusion procedure following Georg et al. (2006b). 20 mg of finely powdered sample was fused with ~200 mg high purity NaOH in silver crucibles at 720 °C for 10 minutes. The crucibles with fusion cakes were sonicated for 30 min in 20 mL doubly-deionized water (DDIW) and left to dissolve for 24 hours. The solution was then transferred into 250 mL polyethylene bottles, carefully rinsing to ensure complete recovery, diluted to 200-250 mL with DDIW, and acidified with 3 mL trace metal grade concentrated HNO_3. Vegetation samples were additionally ashed in Pt crucibles at 450 °C prior to fusion.

Cation-exchange chromatographic separation. Si isotope analyses followed the approach of Georg et al. (2006b). Si was separated from sample matrix by ion exchange chromatography. A 10 mL column was filled with 1.8 mL wet volume BioRad AG50W-X12 (200-400 mesh) resin. The column was washed with a sequence of full column volumes of DDIW followed by a sequence of 3M-6M-10M-6M-3M HCl, and then preconditioning with three column volumes of DDIW. Samples (volumes ranging from 0.05 to ~3 mL) were then loaded onto the column in a ~1% HNO_3 matrix and eluted with 2-5 mL DDIW to obtain a final solution of 0.5 ppm Si (yielding about ~8V (80 pA) for ^{28}Si during analysis). All bracketing standard and reference material aliquots were purified using the same cation-exchange method as the samples. Reference materials (Diatomite, BHVO-2, and Merck Quartz) were processed with the same method. Larger batches of NBS-28 were prepared by eluting with up to 20 mL DDIW.

MC-ICP-MS. Following chromatographic separation of Si, isotope ratios were measured using a Nu Plasma II HR-MC-ICP-MS at the University of Oxford in medium resolution mode, on the flat part of the peak shoulder to avoid $^{14}N^{16}O^+$ interference. For each sample, ratios

were measured over 25 integrations of 10 seconds, repeated in 5 blocks. For each block, the sample analysis was bracketed by measurement of concentration-matched NBS-28 standard solution which had passed through the same column chromatography procedure as the samples. $\delta^{30}Si$ values are reported in ‰ as $^{30}Si/^{28}Si$ sample ratio normalized to the average $^{30}Si/^{28}Si$ ratio of bracketing NBS-28 measurements. The measurement uncertainty is reported as the internal 2σ standard error of sample replicates, or 2σ standard deviation of all NBS-28 bracketing standard measurements within a given analytical session, whichever is higher. Reference materials (diatomite, BHVO-2, and Merck Quartz) were analyzed during sample runs, yielding values of +1.35 ± 0.16‰ (mean ± 2 S.D.; n = 6), –0.28 ± 0.14‰ (n = 5) and –0.01 ± 0.04‰ (n = 3), respectively, all within the ranges reported in previous studies (Reynolds et al., 2007; Abraham et al., 2008; Georg, Zhu, et al., 2009). Comparison of measured $^{30}Si/^{28}Si$ and $^{29}Si/^{28}Si$ ratios indicates good correlation with a slope close to that expected for mass-dependent fractionation (Supplementary Table S2).

2.6 Germanium isotope analysis

River water. 0.5 to 1.0 L of filtered river water containing 6-18 ng of Ge was acidified with distilled HNO_3, and spiked with a Ge isotope double spike ($^{73}Ge/^{70}Ge \approx 1$, previously calibrated and used by Escoube et al. (2012, 2015) and Baronas et al. (2018, 2019)). The spike/sample Ge mass ratio was 1-2, and a purified dissolved $FeCl_3$ salt was added to obtain a Fe concentration of ~0.2 mmol/L. The samples were well mixed, and allowed to equilibrate for at least 16 hours. Next, $Fe(OH)_3$ flock was precipitated by adding Optima-grade NH_4OH until the solution reached a pH of 8-10. The flock was collected by settling and centrifugation, redissolved in 2 mL concentrated Teflon-distilled HNO_3 and diluted to 10 mL with DDIW. The samples were then dried, redissolved in 1 mL concentrated Optima-grade HF and diluted to 30 mL with DDIW to obtain a final 1M HF solution. The samples were then purified through anion exchange columns as described below. The full procedural blank was determined by processing spiked DDIW and ranged from 0.01 to 0.3 ng Ge.

Rocks and sediments. A method adapted from Rouxel et al. (2006) was used for solid sample digestion. 10-130 mg of dried ground sample containing 30-300 ng of Ge was weighed into Teflon digestion vessels and spiked with a Ge isotope double spike ($^{73}Ge/^{70}Ge \approx 1$) in a spike/sample Ge mass ratio of 1-2. The samples were digested by adding 10 mL concentrated Teflon-distilled HNO_3 and heating in a pressurized Teflon vessel at 90 °C for 48h. Then, to ensure the oxidation of any organic matter, 1mL of Optima-grade H_2O_2 was added and digests were heated uncapped at 70 °C until dry. After cooling, 4 mL DDIW and 1mL concentrated trace-metal grade HF were added and samples were digested at 70 °C for 48 h. Replicate digestions done without H_2O_2 yielded the same results, indicating that the presence of organic matter does not interfere with Ge digestion. After cooling, the samples were diluted to 30 mL with DDIW to obtain a final 1M HF solution that was purified through anion exchange columns as described below. The full procedural blank was determined by processing only the Ge double spike and was below 1.7 ng Ge.

Anion-exchange chromatographic separation. A procedure adapted from Rouxel et al. (2006) was used. All reagents used were either in-house Teflon-distilled or Optima-grade. A 10 mL column was loaded with 1.8 mL (wet volume) of BioRad AG1-X8 resin, washed with 10 mL aliquots of 3M HNO_3, 0.28M HNO_3, and DDIW each, then conditioned with 5 mL 1M HF. Samples in 1M HF solution as prepared above were centrifuged to separate insoluble fluorides. The presence or amount of insoluble fluorides at this stage did not appear to affect the final Ge recovery. 10-29 mL of the solution was carefully added to columns. The remaining matrix was eluted with 5 mL of 1M HF followed by 3 mL of DDIW, while fluorinated Ge was retained on the column. Ge was then eluted with 10 mL 0.28M HNO_3. If required, the solution was dried down and redissolved in a smaller volume of 0.28M HNO_3 to obtain the 2-10 ppb Ge concentration required for isotope measurements. Each column was reused 4-5 times, except when retention of DOC from the previous sample was observed based on the color, in which case the resin was replaced. Ge blanks from reused resin were below

detection limit. Ge recovery ranged from 50 to 100%, with loss most likely during the co-precipitation or digestion steps for the fluid and solid samples, respectively. Incomplete recovery does not affect the measured δ^{74}Ge values, as all samples were double-spiked prior to sample preparation. This was confirmed by analyses of certified reference materials BIR-1 and DTS-1 (^{74}Ge = 0.62 ± 0.24 and 0.61 ± 0.07 (n = 2, 2σ), respectively), which had recovery between 60-90% similar to other samples and agreed well with previously measured values (Escoube et al., 2012). Double spike calculations also showed no difference between the full procedural fractionation factors (F_{inst}, including fractionation in the ICP instrument, see Siebert et al. (2001)) of the pure NIST standard and the samples with incomplete recovery.

HG-MC-ICP-MS. Ge isotope analyses were performed on a Thermo Neptune multi-collector ICP-MS at Ifremer using a method adapted from Guillermic et al. (2017). Sample solutions of 2-10 ppb natural Ge in 0.28M HNO_3 were introduced into an online hydride generation system (CETAC HGX-200) at a rate of 150 µL/min where they were mixed with $NaBH_4$ solution introduced at an equal rate. The dissolved $Ge(OH)_4$ species were reduced to gaseous GeH_4 and transported into the ICP-MS torch using Ar carrier gas. The Neptune MC-ICP-MS was operated in low mass resolution mode, measuring ^{70}Ge, ^{72}Ge, ^{73}Ge, and ^{74}Ge in L2, C, H1 and H2 cups, respectively. In addition, L4, L3, L1 and H4 cups were also monitored for ^{68}Zn (possible interference as ^{70}Zn), ^{69}Ga, ^{71}Ga (possible interferences at m/z 70), and ^{77}Se (possible interference as ^{74}Se), respectively. No interferences were detected in any of the runs and therefore no corrections were necessary. The samples were bracketed using a NIST-3120a standard solution that had a total Ge concentration generally within ~20% of the bracketed sample, and was double-spiked to have a spike/sample ratio within ~20% of the bracketed sample. Each sample or standard run consisted of 6 measurement blocks each lasting 2 min (30 cycles of 4 s each), and in most cases 4-5 blocks displaying the most stable signal were retained. Therefore, each measurement represents 8-10 min of counting statistics at signal intensities ranging from 0.4 to 6 V (4-60 pA) at ^{74}Ge (depending on Ge concentration in sample solution, instrument tuning, and freshness of the $NaBH_4$ solution). The δ^{74}Ge values are calculated for each block using the double-spike data reduction routine of Siebert et al. (2001) and are reported in ‰ as ^{74}Ge/^{70}Ge sample ratio normalized to the average ^{74}Ge/^{70}Ge ratio of bracketing NIST 3120a measurements. This method also yields Ge concentration values based on the measured spike/sample ratio. Instrumental blank measurements were generally below 2% of measured sample and standard intensities, suggesting that a wash-out time of 8 min was sufficient to avoid significant memory effects. The measurement uncertainty is reported as the internal 2σ standard error of the used sample blocks, or 2σ standard deviation of all NIST 3120a bracketing standard measurements within a given analytical session, whichever is higher. To confirm accuracy, a number of standard reference materials were digested, chromatographically separated, and analyzed alongside samples, as reported previously by Baronas et al. (2018). Analyses of reference materials yielded values that agree well with previous literature (0.58± 0.06‰ for DTS-1, 0.53 ± 0.08‰ for BIR-1, and 0.55 ± 0.15‰ for BHVO-1).

3 Results

3.1 Soil and clay chemistry and mineralogy

The fresh andesite rock samples (considered representative of bedrock) are comprised of ~50-60 wt% SiO_2, 15 wt% Al_2O_3, 6-10 wt% Fe_2O_3, and other major oxides ranging between 1–8% each (Table 1, Fig. S1). Relative to this parent bedrock, the bulk soils and separated clays sampled at two soil pits were strongly desilicified (20-28 wt% SiO_2), enriched in Al_2O_3 (27-35%) and Fe_2O_3 (15-18%), and strongly depleted in all major cations (< 1% of Na_2O, K_2O, CaO, and MgO). There were no significant differences between the two soil pits (A4 and L6). These results are consistent with previous studies, which identified the strongly weathered character of these soils, with clay-sized fraction between 67 and 83% and relatively invariant in the top 2 m (Kautz & Ryan, 2003; Kleber et al., 2007). In terms of major oxide chemistry, the separated clays are chemically indistinguishable from bulk soils (Table 1, Fig. S1). Using qualitative powder XRD (Proto AXRD at the Natural History Museum of Los An-

geles), the major mineral phases were found to be gibbsite, kaolinite/halloysite, and goethite, as well as traces of magnetite (data not shown). These results are consistent with a previous study of soil mineralogy at these sites (Kleber et al., 2007). There were no distinguishable differences in mineralogy between separated clays and bulk soils, except that a small amount of residual quartz was present in the bulk soil samples.

3.2 Fluid chemistry

Major and trace element concentrations in La Selva streams and groundwater seeps spanned a wide range of values (Table 2). Local rainwater reflected seawater aerosol inputs (Na and Cl concentrations of ~ 60 μmol/L), whereas Ge and Si concentrations were low (4 μmol/L and 9 pmol/L, respectively) with Ge/Si of 2.3 μmol/mol. Samples of soil pore water and shallow groundwater from local wells were dilute and similar to rainwater with regards to major cation and anion concentrations, with the exception of slightly higher Ca and Mg (10-80 μmol/L in most cases) and significantly higher Si and Ge (50-140 μmol/L and 90-140 pmol/L, respectively). In contrast, local La Selva streams ranged from very dilute and similar to local groundwaters (e.g. Taconazo stream) to very concentrated, with Si and Na up to 1300 μmol/L, Mg - 1100 μmol/L, Ca - 600 μmol/L, and Cl - 700 μmol/L (e.g. El Salto catchment) and similar in composition to solute-rich interbasin groundwater, represented by a sample of Guacimo spring (CR05) collected ~1 km south of the La Selva Biological station (Fig. 1).

3.3 Ge and Si element and isotope distribution

The Ge and Si isotope composition and the Ge/Si ratios of various sample types in the La Selva soils are summarized in Fig. 2 and Tables 1 and 2. The bedrock exhibits Ge/Si of 2.2±0.1 μmol/mol, typical of volcanic rocks, whereas bulk soils show strongly elevated Ge/Si ratios of 6-6.5 μmol/mol, typically associated with secondary minerals such as kaolinite and Fe oxides (Mortlock & Froelich, 1987; Kurtz et al., 2002). The separated clays are further enriched in Ge/Si, reaching values of 6.7-7.8 μmol/mol, consistent with higher degree of Ge retention relative to Si during chemical weathering (see Section 4.4). In contrast, all fluids exhibit lower Ge/Si ratios with a local groundwater range of 1.4-2.0 μmol/mol, interbasin groundwater at 0.3 μmol/mol, and La Selva streams ranging widely between these extremes (0.4-1.3 μmol/mol).

Isotopically, all analyzed materials are significantly fractionated relative to the starting bedrock. The bulk soils are strongly depleted in heavy Si isotopes ($\delta^{30}Si_{soil}$ = -1.7 to -2.5‰) and the separated clays are depleted further still ($\delta^{30}Si_{clay}$ = -2.4 to -2.7‰), relative to the parent bedrock ($\delta^{30}Si_{bedrock}$ = -0.1‰). Two different unidentified plant species that exhibit very different degrees of Si content (SiO_2 weight fraction of 1.0 and 24%; Table 1) are isotopically light and indistinguishable from each other ($\delta^{30}Si_{veg}$ = -1.8 to -1.9‰). La Selva groundwater and pore water composition is heavier than the bulk soils but in most cases still lighter than the parent bedrock ($\delta^{30}Si_{pw}$ = -1.3 to 0.2‰; Fig. 2c). Interbasin groundwater is heavy at 1.0± 0.2‰, while La Selva streams span a wide range of values from 0.2 to 1.2‰, correlating with major solute concentrations and Ge/Si ratios (see discussion below).

Similarly to $\delta^{30}Si$, light Ge isotopes are enriched in soils and clays ($\delta^{74}Ge$ = -0.1 to -0.3‰) relative to parent bedrock ($\delta^{74}Ge_{bedrock}$ = 0.6‰), whereas local groundwater (2.2 ‰), interbasin groundwater (4.0 ‰) and local streams (2.4-3.6 ‰) are all isotopically heavy relative to bedrock (Fig. 2b). Ge/Si, $\delta^{30}Si$, and $\delta^{74}Ge$ composition of bulk soils, separated clays, and soil pore waters are all relatively constant with depth within uncertainty (Fig. 2). A crossplot of $\delta^{30}Si$ vs. Ge/Si and vs. $\delta^{74}Ge$ for all samples measured in this study is given in the Supplementary Material (Fig. S6).

[htbp]

Table 1. Chemical composition of solids sampled at La Selva Biological Station. No measurements were made where values are not given.

Sample	Depth	ID	Al_2O_3 (wt%)	Fe_2O_3 (wt%)	SiO_2 (wt%)	Na_2O (wt%)	K_2O (wt%)	CaO (wt%)	MgO (wt%)	MnO (wt%)	TiO_2 (wt%)	Th (µg/g)	Zr (µg/g)	Ge (µg/g)	Ge/Si (µmol/mol)	$\delta^{30}Si$ (‰)	$\delta^{74}Ge$ (‰)
Bedrock																	
Rock 1	--	LS-R1	14.1	5.7	61.7	4.00	3.61	3.97	1.72	0.14	1.03	16.6	311	1.54	2.07	-0.13 ± 0.18	0.64 ± 0.08
Rock 2	--	LS-R2	14.1	9.3	53.8	2.43	1.25	8.30	5.73	0.15	1.12	4.8	120	1.52	2.34	-0.09 ± 0.25	0.54 ± 0.02
Bulk soils																	
Soil pit A4	0 cm	A4-0-B	27.1	15.2	20.9	0.05	0.26	0.17	0.36	0.11	2.02	13.2	282	1.55	6.16	-1.74 ± 0.21	-0.22 ± 0.15
Soil pit A4	50 cm	A4-50-B	35.1	17.1	27.1	0.04	0.25	0.03	0.29	0.19	2.19	16.6	342	--	--	-2.11 ± 0.23	--
Soil pit A4	100 cm	A4-100-B	--	--	--	--	--	--	--	--	--	--	--	1.87	6.00	--	-0.16 ± 0.08
Soil pit A4	200 cm	A4-200-B	34.2	18.3	28.4	0.03	0.13	0.02	0.24	0.08	2.39	17.5	368	2.22	6.48	-1.88 ± 0.16	-0.08 ± 0.08
Soil pit L6	0 cm	L6-0-B	31.1	17.4	21.3	0.05	0.18	0.06	0.32	0.04	2.00	13.6	284	1.63	6.33	-2.05 ± 0.19	-0.28 ± 0.27
Soil pit L6	50 cm	L6-50-B	34.8	17.9	25.7	0.03	0.15	0.02	0.26	0.04	2.05	15.0	306	1.95	6.30	-2.19 ± 0.18	-0.08 ± 0.08
Soil pit L6	200 cm	L6-200-B	31.1	15.8	25.9	0.02	0.13	0.01	0.18	0.03	1.82	15.3	287	2.08	6.63	-2.47 ± 0.25	0.07 ± 0.04
Separated clays																	
Soil pit A4	0 cm	A4-0-C	32.9	15.7	22.4	0.08	0.62	0.23	0.27	0.13	1.66	14.7	299	1.95	7.21	-2.60 ± 0.23	-0.27 ± 0.05
Soil pit A4	200 cm	A4-200-C	34.7	16.5	27.3	1.31	0.12	0.02	0.18	0.06	1.94	19.0	356	2.56	7.76	-2.44 ± 0.07	-0.06 ± 0.08
Soil pit L6	0 cm	L6-0-C	32.9	17.1	23.3	0.09	0.25	0.06	0.21	0.03	1.77	15.0	307	2.16	7.69	-2.69 ± 0.15	-0.20 ± 0.13
Soil pit L6	200 cm	L6-200-C	35.0	17.0	27.8	0.54	0.15	0.01	0.16	0.03	2.02	17.9	363	2.27	6.74	-2.37 ± 0.09	-0.12 ± 0.08
Vegetation																	
Above A4	--	A4-V	--	--	1.0	--	--	--	--	--	--	0.5	--	--	--	-1.90 ± 0.11	--
Above L6	--	L6-V	--	--	23.7	--	--	--	--	--	--	0.3	--	--	--	-1.78 ± 0.19	--
Bedload																	
LS01 (bulk)	--	LS01-B	22.5	9.7	28.4	0.68	0.63	1.72	0.81	0.12	1.49	15.3	302	--	--	-1.44 ± 0.09	--
LS01 (clay)	--	LS01-C	--	--	--	--	--	--	--	--	--	--	--	--	--	-2.52 ± 0.13	--
LS02 (bulk)	--	LS02-B	23.1	9.9	36.6	1.28	1.08	2.98	1.44	0.08	1.42	15.2	296	--	--	-1.06 ± 0.07	--
Suspended load																	
LS01	0 m	LS01-S	27.8	12.5	29.6	0.28	0.41	0.52	0.33	0.07	1.63	19.9	404	--	--	-1.91 ± 0.17	--
LS02	0 m	LS02-S	27.6	15.4	33.6	1.06	1.01	2.16	1.00	0.08	1.61	21.4	57	--	--	-1.34 ± 0.17	--
LS04	0 m	LS04-S	28.4	17.5	3.7	0.32	0.20	0.54	0.23	0.19	1.61	21.2	137	--	--	-2.37 ± 0.12	--
LS15	0 m	LS15-S	33.0	15.1	12.7	0.05	0.18	0.10	0.15	0.06	2.11	30.6	648	--	--	-2.59 ± 0.14	--

Table 2. Chemical composition of fluids sampled at La Selva Biological Station. No measurements were made where values are not given.

Sample	Details	ID	Temp. (°C)	pH	Cond. (µS)	Alk. (meq/L)	Si (µM)	Na (µM)	Mg (µM)	K (µM)	Ca (µM)	Cl (µM)	SO_4 (µM)	Al (nM)	Fe (nM)	Ge (pM)	Ge/Si (µmol/mol)	$\delta^{30}Si \pm 2\sigma$ (‰)	$\delta^{74}Ge \pm 2\sigma$ (‰)
Rainwater		LS16	--	--	--	--	4	60	8	4	5	60	13.4	399	194	9	2.3	--	--
Streams & groundwater seeps																			
Taconazo	at weir	LS01	25.1	5.6	9	0.06	120	60	12	9	14	53	6.5	644	689	107	0.89	0.29 ± 0.13	2.58 ± 0.12
Arboleda	at weir	LS02	24.9	6.5	276	2.49	1070	768	533	125	400	355	46.1	431	649	423	0.40	1.03 ± 0.12	3.25 ± 0.12
El Salto	east trib.	LS04	24.4	6.5	16	0.15	232	93	22	--	29	51	5.8	409	449	88	0.38	0.46 ± 0.18	3.05 ± 0.12
El Salto	gw. seep	LS05	25.3	6.7	424	4.07	1260	1250	877	173	529	619	76.8	843	164	498	0.39	1.27 ± 0.21	--
El Salto	tributary	LS06	25.8	6.6	233	4.68	1290	1340	1080	236	624	678	86.3	265	225	505	0.39	1.12 ± 0.14	3.61 ± 0.12
El Salto	main stem	LS07	25.2	7.1	157	1.22	550	464	327	74	209	237	28.5	643	832	231	0.42	1.03 ± 0.10	3.35 ± 0.12
El Sura	main stem	LS08	25.5	6.6	10	0.09	167	72	18	16	19	46	5.2	274	380	90	0.54	0.57 ± 0.15	--
Piper	main stem	LS09	25.4	6.0	13	0.12	151	67	24	9	28	50	5.7	266	478	89	0.59	0.70 ± 0.14	--
Quebrada Esquina		LS10	25.1	6.8	21	0.20	284	96	31	31	42	52	5.1	1190	511	104	0.37	0.92 ± 0.26	3.02 ± 0.12
El Saltito	gw. seep	LS11	25.1	6.0	6	0.04	196	64	8	16	8	49	5.2	475	502	131	0.67	0.67 ± 0.27	2.63 ± 0.12
Taconazo	at weir	LS12	--	--	10	0.06	143	60	13	11	15	50	5.2	319	299	103	0.72	0.64 ± 0.20	--
Arboleda	at weir	LS13	--	--	142	3.10	1140	839	583	139	439	379	49.0	638	569	455	0.40	1.23 ± 0.15	--
Taconazo	upstream	LS14	25.7	5.4	10	0.02	77	60	13	15	12	59	9.5	907	549	97	1.26	0.38 ± 0.15	2.39 ± 0.12
Arboleda	upstream	LS15	26.2	5.4	14	0.02	88	65	16	22	12	62	14.2	781	278	101	1.14	0.19 ± 0.09	2.60 ± 0.12
El Saltito	main stem	LS17	--	--	117	0.94	423	307	209	45	144	167	21.5	661	739	188	0.44	1.03 ± 0.13	--
Large rivers																			
Rio Sarapiqui	at Puerto Viejo	CR01	27.2	7.2	50	0.43	279	--	--	--	--	58	34.2	1680	847	136	0.49	1.32 ± 0.14	--
Rio Sarapiqui	at Sardinal	CR02	25.8	7.1	27	0.39	295	--	--	--	--	114	180.0	565	168	120	0.41	1.34 ± 0.26	--
Rio Sarapiqui	at San Miguel	CR03	22	8.0	117	0.87	684	--	--	--	--	94	158.4	2050	544	177	0.26	1.52 ± 0.21	--
Interbasin groundwater																			
Guacimo	spring ("old")	CR05	25.4	6.4	590	--	1300	1340	1490	--	757	733	125.8	308	366	405	0.31	1.02 ± 0.24	4.02 ± 0.12
Local groundwater (wells)																			
Farm	--	LS03	25.1	5.2	20	0.04	51	70	8	--	23	60	18.2	324	472	97	1.91	0.06 ± 0.13	2.24 ± 0.12
Taconazo	--	LS18	--	--	--	--	74	56	11	3	13	53	9.5	1920	119	99	1.35	0.17 ± 0.14	--
Saltito	60 cm	LS19	--	--	--	--	53	71	22	7	25	49	7.5	5920	735	92	1.75	0.21 ± 0.18	--
Salto	60 cm	LS20	--	--	--	--	69	60	16	6	16	53	7.6	2070	587	135	1.97	-0.67 ± 0.07	--
Salto	100 cm	LS21	--	--	--	--	87	84	17	--	17	52	8.5	17600	3980	--	--	-0.40 ± 0.26	--
Soil pore water																			
Soil pit A4	0 cm	A4-0-W	--	--	--	--	72	122	62	--	175	63	44.8	12040	--	--	--	-1.25 ± 0.08	--
Soil pit A4	25 cm	A4-25-W	--	--	--	--	52	87	18	--	59	66	22.5	294	--	--	--	-1.02 ± 0.10	--
Soil pit A4	50 cm	A4-50-W	--	--	--	--	53	101	22	--	62	56	26.3	295	--	--	--	-1.21 ± 0.08	--
Soil pit A4	200 cm	A4-200-W	--	--	--	--	45	67	23	--	52	73	12.6	915	--	--	--	-0.96 ± 0.09	--
Soil pit L6	0 cm	L6-0-W	--	--	--	--	139	120	50	--	79	103	35.1	23900	--	--	--	-0.03 ± 0.11	--
Soil pit L6	50 cm	L6-50-W	--	--	--	--	43	81	13	--	32	69	17.5	331	--	--	--	-1.04 ± 0.08	--
Soil pit L6	200 cm	L6-200-W	--	--	--	--	33	54	10	--	36	40	18.8	61	--	--	--	0.02 ± 0.10	--

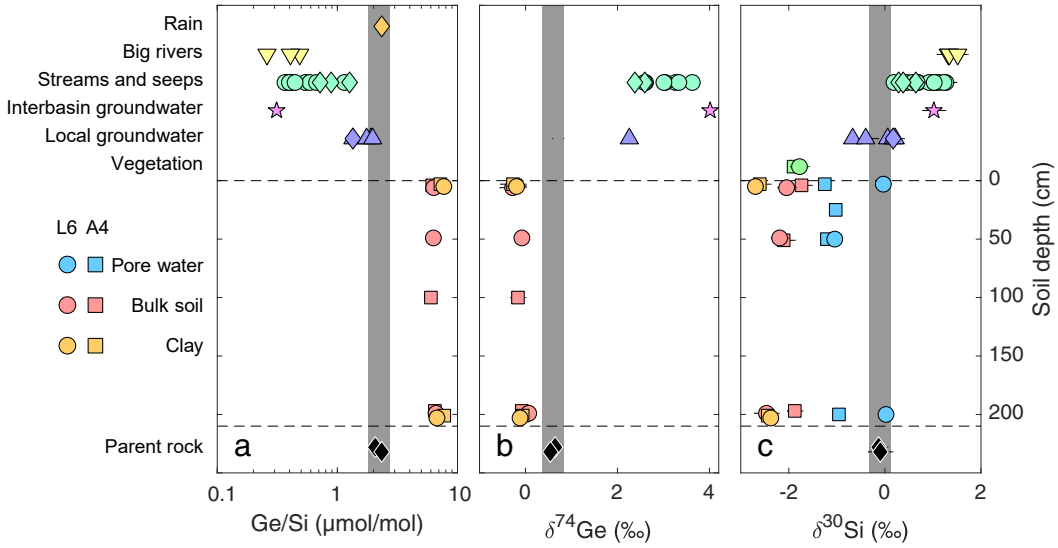

Figure 2. Silicon and germanium isotope and Ge/Si ratios of all samples in this study. The depth scale (y-axis) on the right applies to the bulk soil, separated clay, and pore water samples only. Taconazo watershed stream and well samples are shown as teal diamonds. Where not visible, 2σ error bars are smaller than the symbols.

4 Discussion

The results of this study are consistent with the recent findings of the close coupling between Ge/Si, δ^{30}Si, and δ^{74}Ge in the terrestrial environment (Baronas et al., 2018). All three proxies primarily reflect fractionation during weathering, with secondary phases enriched in light isotopes and Ge relative to Si (Table 1), leaving fluids with isotopically heavier and low Ge/Si signatures (Table 2). In addition, vegetation uptake affects dissolved Ge/Si and δ^{30}Si signatures (e.g., Cornelis et al., 2010), while it appears to have a smaller (but poorly quantified) effect on δ^{74}Ge (Baronas et al., 2018). Importantly, our study site at La Selva represents an advanced chemical weathering environment with both the bulk soils and the local soil and stream waters showing some of the lightest Ge and Si isotope compositions measured to date.

Below, we discuss 1) the role of mixing between lowland fluids and interbasin groundwater in controlling the chemical and isotopic signatures of streams in this study area; 2) Ge and Si isotope fractionation during the weathering of volcanic lavas by interbasin groundwater, informed by a kinetic reactive transport model; 3) the relative importance of mineral vs. vegetation controls on Ge and Si isotopic signatures in La Selva lowlands, quantified using a simple mass balance model; and 4) the global relationship between the weathering intensity (chemical depletion) recorded in secondary weathering products (bulk soils and clays) and their Ge/Si, δ^{30}Si, and δ^{74}Ge signatures.

4.1 Stream chemistry controlled by mixing of local fluids and volcanic interbasin groundwater

Regarding La Selva streams, it has been established by previous workers that the first order control on their composition is the mixing of dilute lowland surface water with solute-rich volcanic interbasin groundwater (IBGW) sourced from higher elevation on the slopes of Barva Vulcano (e.g., Pringle et al., 1990; Genereux & Jordan, 2006; Genereux et al., 2009), some tens of kilometers south of the study site (Fig. 1). Our most representative sample of IBGW is from Guacimo spring (CR05), exhibiting Si, Na, and Cl concentrations of 1.30, 1.34,

and 0.73 mmol/L, respectively. Previous work showed the composition of this spring to be stable over several years of varying hydrological conditions (Na = 1.92±0.44 mmol/L, Cl = 0.90±0.10 mmol/L, n = 56; Genereux et al. (2002)). Within the La Selva research station, IBGW input affects each stream to a different degree and its influence can also vary within a watershed. This heterogeneity is well exemplified by comparing two streams where samples were taken at different points along each stream (Table 2). In the Taconazo watershed, the upstream chemistry (LS14) is very similar to the outlet (LS01/LS12), consistent with negligible contribution from IBGW, whereas in the Arboleda watershed, the upstream fluid (LS15) is very similar to the Taconazo, but the stream water sampled at the outlet (LS02) is highly enriched in solutes and closely resembles the chemistry of pure IBGW end-member, exemplifying the localized IBGW discharge in the lowlands of the La Selva Biological Station.

The first order variability of the whole stream chemistry dataset can therefore be described in terms of a mixing relationship between a dilute local water end-member and a solute-rich IBGW end-member, observed clearly in Na-Cl mixing space (Fig. 3a). In Ge-Cl and Si-Cl mixing space (Fig. 3b-c), it is clear that not all dissolved Ge and Si is derived from IBGW because local streams plot on a mixing line between IBGW and local soil waters (rather than rainwater), which act as a supply of Ge and Si sourced from the weathering of lowland soils.

Interestingly, some La Selva streams fall outside of the mixing space between local soil waters and IBGW, indicating another source of Si (and to lesser extent, Ge). This source appears to have a low Ge/Si ratio and a relatively low Cl content, compared to IBGW, and seems to have a higher contribution in the large Rio Sarapiqui River (Fig. 3b). We speculate that it might represent weathering closer to regolith-bedrock interface, some tens of meters deeper than our 2m-deep soil pits. Ultimately all local fluids likely lie on a continuous spectrum of composition between the shallow and the deep weathering signatures.

Importantly, the Si isotope composition of lowland streams lies almost exclusively on the two end-member mixing trend between shallow soil waters and IBGW (Fig. 3d). This suggests that deeper weathering fluids have limited influence on δ^{30}Si signatures of local streams, relative to the first-order control by mixing with IBGW. The evolution of Ge and Si signatures in La Selva weathering fluids can therefore be summarized as follows. Dilute rainwater percolates shallow soils, where weathering (and potentially organic litter decomposition) adds a relatively small net amount of dissolved Ge and Si. Some portion of these fluids percolate to the regolith interface where they may gain additional Si. Finally, depending on particular catchment and location, some of these local fluids are mixed with varying proportions of IBGW, resulting in the wide range of sampled compositions.

In the following Sections 4.2-4.3 we focus on understanding the processes that control the compositions of the two contrasting end-member fluids: the volcanic interbasin groundwater and the shallow lowland soil water.

4.2 Modeling Ge and Si isotope fractionation in interbasin groundwater

The interbasin groundwater (IBGW) is thought to percolate through extensive layered volcanic tuff aquitards as it descends into the lowlands where the La Selva study area is located (Genereux et al., 2009). The δ^{30}Si signature of IBGW is similar to that observed in other weathering environments where secondary clay precipitation during silicate weathering results in isotopically heavy river or ground water (e.g., Ziegler et al., 2005; Georg et al., 2006a; Hughes et al., 2013; Frings et al., 2016). It must be noted that isotopically light groundwater signatures have also been documented elsewhere, likely reflecting the dissolution of secondary clays in the sedimentary rock-hosted aquifers (Georg, Zhu, et al., 2009; Georg, West, et al., 2009; Pogge von Strandmann et al., 2014). The low Ge/Si ratio of 0.3 μmol/mol in IBGW is also consistent with significant secondary mineral precipitation (Murnane & Stallard, 1990; Froelich et al., 1992). While there are no previous published groundwater δ^{74}Ge data available for comparison, the heavy signature of IBGW is consistent with the broad negative correlation between Ge/Si and δ^{74}Ge observed by Baronas et al. (2018) in global rivers.

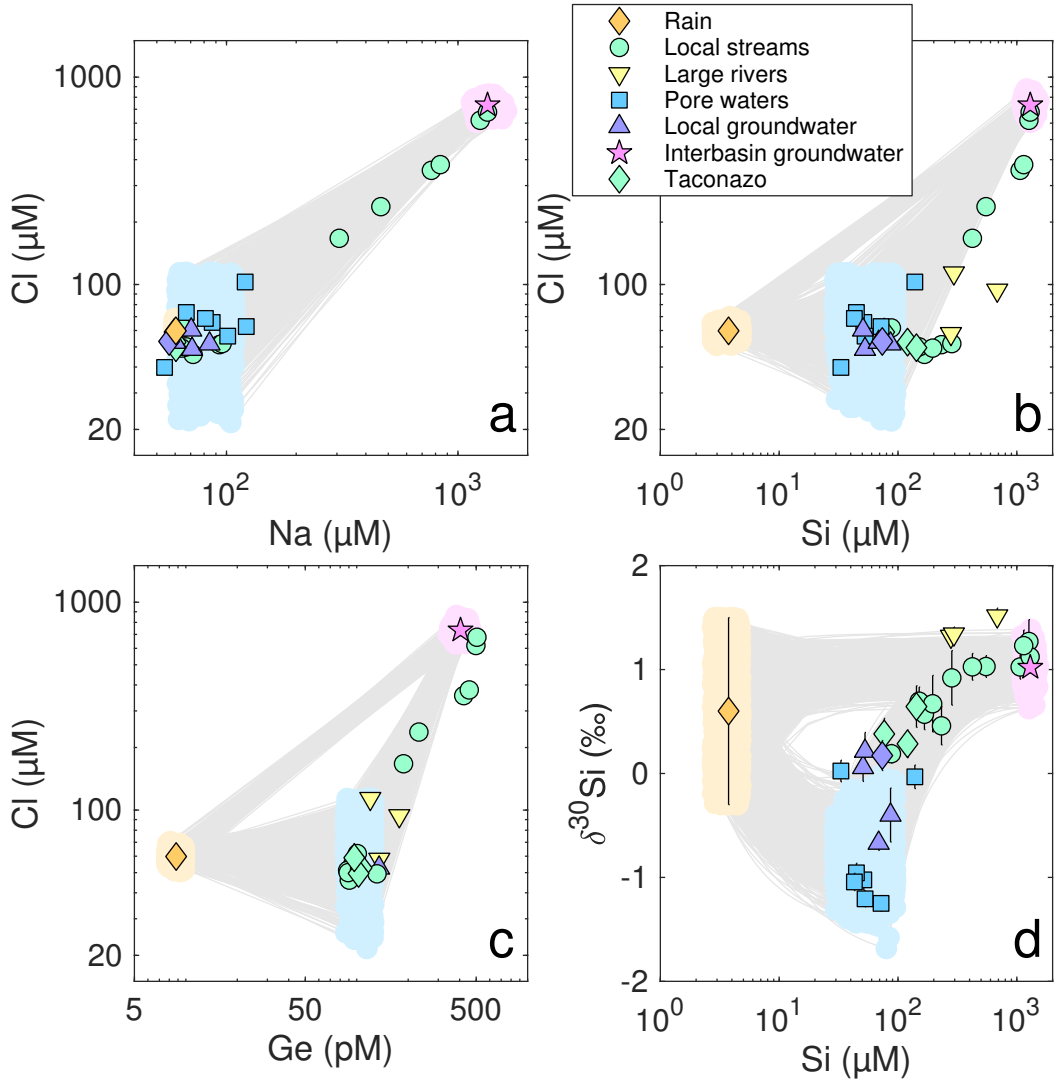

Figure 3. The range of chemical and δ^{30}Si compositions in La Selva streams. In each panel, the gray area shows the mixing space between rainwater, lowland weathering fluids (all pore waters and well samples), and interbasin groundwater (Guacimo spring sample CR05, pink star). The mixing space is calculated from 1000 Monte Carlo simulations, randomly sampling each end-member (shaded area around the measured sample compositions of the three end-members). For rainwater, δ^{30}Si was not measured; therefore, for visualization purposes, a range of values anywhere between -0.3 and 1.5‰ was assigned, encompassing most measured silicate rock and seawater values (Frings et al., 2016).

Based on ^{14}C dating of dissolved organic carbon, the transit time of IBGW is longer than 2000 years, although this estimate might be affected by partial isotopic exchange with magmatic CO_2 (Genereux et al., 2009). Nevertheless, such long fluid transit timescale suggests that IBGW fluids may have reached a chemical and isotopic equilibrium with the reactive volcanic rock and the precipitating secondary phases by the time they discharge at La Selva, which is also consistent with the inter-annually stable solute concentrations of IBGW (Genereux & Jordan, 2006). In order to test whether this is likely to be the case, we adapted a reactive transport model initially developed to investigate U-Th series isotopes in groundwater by Tricca et al. (2000) and Porcelli (2008) and later applied to Li isotopes by Pogge von Strandmann et al. (2014). The details of the model are described and the derivation of key equations is given in the Supplementary Material Text S1.

To obtain a conservative estimate of fluid equilibration timescale, we used a mineral dissolution rate constant (10^{-16} mol m^{-2} s^{-1}) that is at the lower end of field-derived plagioclase weathering rates (Brantley et al., 2008). Including a simple representation of thermodynamic control on rates based on transition state theory (e.g., Schott et al., 2009), we calculated that IBGW fluids should reach steady state (with regards to both Si and Ge concentrations and their isotopic compositions) within less than 600 years, or about 2 km of subsurface flow (see Supp. Fig. S4), whereas the minimum distance between IBGW recharge area and La Selva is estimated to be ~9 km, ignoring tortuosity of the subsurface flowpaths (Genereux et al., 2009). At steady state, the isotopic difference between the IBGW fluid and the volcanic rock with which it had equilibrated should directly reflect the fractionation factor associated with Si and Ge removal from solution into secondary phases during groundwater transit (e.g., $\Delta^{30}Si_{sec-diss} = \delta^{30}Si_{rock} - \delta^{30}Si_{IBGW}$). Using the mean isotopic composition of the IBGW-dominated fluids (i.e. samples LS02, LS05, LS06, LS13, and CR05; Table 2) yields the following isotope fractionation factors: $\Delta^{30}Si_{sec-diss} = -1.2 \pm 0.3$‰ and $\Delta^{74}Ge_{sec-diss} = -3.0 \pm 0.9$‰. It must be noted that this model does not make an implicit assumption on the removal mechanism (e.g., co-precipitation vs. net adsorption), with the only implication being that it is a first-order kinetic process.

Because the reactive transport model tracks the amount of Si and Ge removed from solution, it can be used to calculate the fraction of total dissolved Si and Ge remaining in the final IBGW fluid ($f_{diss}Si = 0.25$, $f_{diss}Ge = 0.03$) and the accumulated secondary phase composition ($\delta^{30}Si_{sec} = -0.49$‰, $\delta^{74}Ge_{sec} = 0.49$‰; Fig. S4). Applying the often used steady state equilibrium model ($\Delta_{sec-diss} = \delta_{sec} - \delta_{diss}$; Johnson et al. (2004); Bouchez et al. (2013)) to these values yields fractionation factors $\Delta^{30}Si_{sec-diss} = -1.6$‰ and $\Delta^{74}Ge_{sec-diss} = -3.2$‰, respectively. The agreement between these values and the measured difference between initial rock composition and the final IBGW fluid ($\Delta^{30}Si_{sec-diss}$ and $\Delta^{74}Ge_{sec-diss}$ values given above) provides additional support that the kinetic reaction rates and other parameters used in the model (Table S3) are not unreasonable. Both Si and Ge isotope fractionation factors calculated here are within the range of values determined previously for a number of global rivers (Baronas et al., 2018), as well as experimental adsorption or co-precipitation with a range of secondary phases in the case of Si (Delstanche et al., 2009; Oelze et al., 2014, 2015; Frings et al., 2016) and with Fe oxides in the case of Ge (Pokrovsky et al., 2014).

4.3 Lowland critical zone processes

The small watersheds in the La Selva lowlands represent a weathering regime that is very different from the interbasin groundwater system. Due to the warm and humid tropical climate combined with low denudation rates, the soils of La Selva are entirely depleted of primary minerals (with the exception of some unreactive quartz) and major cations, and therefore represent an extreme example of a supply-limited weathering regime (see Section 3.1). Progressive weathering has resulted in the formation of thick (up to 20m) oxisols that are enriched in light Si and Ge isotopes (Fig. 2). Soil pore water Si concentrations indicate that these soils are in the process of being further slowly desilicified and soil clays (dominantly kaolinite) are in the process of being converted into neoformed poorly crystalline Al-Si-Fe phases (Kleber et al.,

2007), which results in further fractionation of $\delta^{30}Si$, $\delta^{74}Ge$, and Ge/Si. In this section, we explore how these tracer signatures are currently generated in the lowland soil waters and streams unaffected by interbasin groundwater inputs (Fig. 2). Using a simple isotope mass balance model, we obtain a snapshot of the current, "short-term" Ge and Si cycle on a soil profile scale.

4.3.1 Partitioning and fractionation of Si and Ge between different mass reservoirs

On a soil profile scale, water inputs are spatially distributed and flowpaths are short, on the scale of meters, making a single flowpath reactive-advective model such as that applied to IBGW (Section 4.2) unsuitable. Instead, we employ a simple mass balance (a.k.a., "mixed open system") model, recently developed for the coupled Ge/Si-isotope system and applied on a catchment-scale by Baronas et al. (2018). We use it to understand the fate of Si and Ge released from the soils during chemical weathering, partitioning it between export in the dissolved phase (pore water), uptake by neoforming phases (which we refer to as "clays" from here on for simplicity, emphasizing the separation methodology, while acknowledging that they likely contain both aluminosilicate and oxide phases), and uptake by the abundant tropical vegetation. This framework is impartial to the exact isotope fractionation mechanism (kinetic or equilibrium) and assumes that the system (soil profile) as a whole is at a (quasi) steady state, i.e., any change in the chemical composition of the different solid reservoirs is slow relative to the timescale at which the pore water composition attains its signature (Bouchez et al., 2013). In other words, the isotopic composition of the mineral and vegetation reservoirs is deemed stable over fluid transit timescales. The steady state, however, does not imply a chemical or isotopic equilibrium between the different phases.

The model is described in detail in Baronas et al. (2018) and only slightly modified here to make better use of the clay and vegetation data collected in this study (see description in Supp. Material 1). Briefly, we use the Si/Na and Ge/Na ratios in the dissolving material (represented by the sampled bulk soils) and the fluids (represented by the sampled soil pore waters) to determine the partitioning of Si and Ge fluxes between the fraction taken up by vegetation and neoforming clays and that remaining in solution (f^{Si}_{diss} and f^{Ge}_{diss}). Next, we use the $\delta^{30}Si$ composition of the three phases to determine the exact partitioning of Si uptake between clays (f^{Si}_{sec}) and vegetation (f^{Si}_{bio}). Finally, we use the Ge/Si composition of the dissolved and clay phases to determine Ge uptake partitioning between clays (f^{Ge}_{sec}) and vegetation (f^{Ge}_{bio}). We use the Monte Carlo method to estimate the uncertainty of the calculated parameters. The model is run 10 million times, randomly sampling from within the uncertainties of all the input parameters (Supp. Table S4). The model results are summarized in Supp. Table S5. At steady state, the isotopic fractionation factors are equal to our measured difference in isotopic composition of the three phases, namely:

$$\Delta^{30}Si_{sec-diss} = \delta^{30}Si_{clay} - \delta^{30}Si_{porewater} \quad (1)$$

$$\Delta^{30}Si_{bio-diss} = \delta^{30}Si_{veg} - \delta^{30}Si_{porewater} \quad (2)$$

$$\Delta^{74}Ge_{sec-diss} = \delta^{74}Ge_{clay} - \delta^{74}Ge_{porewater} \quad (3)$$

yielding values of $\Delta^{30}Si_{sec-diss} = -1.7 \pm 0.5$‰, $\Delta^{30}Si_{bio-diss} = -1.0 \pm 0.5$‰, and $\Delta^{74}Ge_{sec-diss} = -2.3 \pm 0.2$‰ (median ± 1 std. dev.).

Detailed mineralogical studies of the soils discussed here indicate the ongoing conversion of kaolinite into mostly amorphous Al-Si oxides (some combination of allophane, halloysite, and/or gibbsite) (Sollins et al., 1994; Kautz & Ryan, 2003; Kleber et al., 2007). Multiple recent experimental studies have shown that $\Delta^{30}Si_{sec-diss}$ fractionation factors associated with amorphous silica and Si-Al oxide precipitation can range from -5 to 0 ‰, with higher fractionation induced by far-from-equilibrium conditions (Oelze et al., 2014, 2015; Roerdink et al., 2015; Fernandez et al., 2019). Similarly, $\Delta^{74}Ge_{sec-diss}$ during reversible Ge adsorption onto Fe (oxy)hydroxides was smaller (-1.7 ‰) than during irreversible co-precipitation (down

to -4.4 ‰), likely representing dominantly close to equilibrium and far-from-equilibrium conditions, respectively (Pokrovsky et al., 2014). Our results therefore suggest incomplete Si (and possibly Ge) isotope equilibration between pore waters and neoforming solids in the soils studied here.

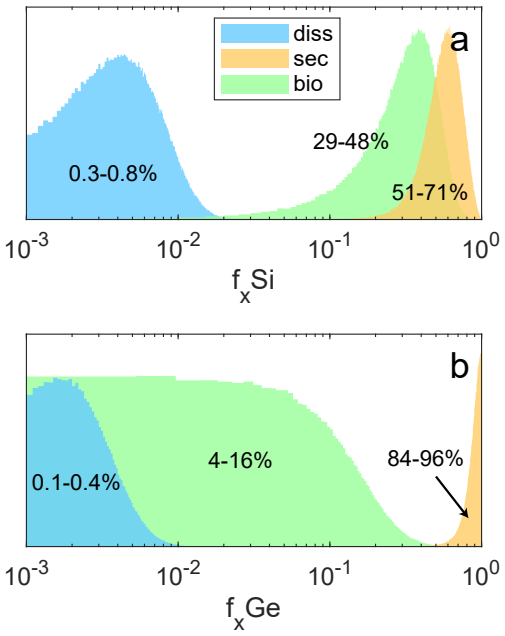

Figure 4. Partitioning of (a) Si and (b) Ge reservoirs in the studies soils of La Selva lowlands, between the dissolved (f_{diss}Si and f_{diss}Ge), neoformed clay (f_{sec}Si and f_{sec}Ge), and vegetation (f_{bio}Si and f_{bio}Ge) fractions. Results are shown as normalized probability distributions of the Monte Carlo model results (see Section 4.3.1 and Supp. Material 1).

In addition to isotopic fractionation, this model yields estimates of Ge/Si fractionation associated with clay and vegetation uptake of the two elements. We calculate $\alpha_{sec}^{Ge/Si}$ = 3.4± 1.0 (defined as $(Ge/Si)_{sec}/(Ge/Si)_{diss}$; Baronas et al. (2018)) or K_{sec} = 1.5 ± 0.3 (defined as $(Ge/Si)_{sec}/(Ge/Si)_{ini}$, equivalent to K_w in Froelich et al. (1992), where $(Ge/Si)_{ini}$ is the composition of the dissolving minerals, in this case represented by bulk soils). Similarly, the biological fractionation factor $\alpha_{bio}^{Ge/Si}$ = 0.62 ± 0.28 (defined as $(Ge/Si)_{veg}/(Ge/Si)_{diss}$). Calculated independently of any Ge/Si measurements in vegetation, this value is nevertheless in line with previous studies, which had shown a similar degree of discrimination against Ge by plants (Blecker et al., 2007; Delvigne et al., 2009; Cornelis et al., 2010; Meek et al., 2016)).

Although the Ge/Si composition of secondary phases precipitating during interbasin groundwater flow cannot be measured directly, it can be calculated using the reactive transport model (Supp. Material 1), yielding 3.9–4.1 µmol/mol, and thus an $\alpha_{sec}^{Ge/Si}$ value of 10±1. The $\alpha_{sec}^{Ge/Si}$ values determined in both the IBGW and lowland soil environments here are in agreement with the global range of values (2-22) reported by Baronas et al. (2018) using data from catchments of different sizes from around the world.

Finally, the main purpose of our model is to calculate how the release of Si and Ge from soils via weathering is partitioned between the three phases, namely neoformed clays, vegetation (primarily phytoliths), and solution. The results (Fig. 4) show that the majority of Si is taken up by neoforming clays (f_{sec}Si = 61 ± 14%), with a significant portion taken up by

vegetation ($f_{bio}Si$ = 39±14%) and only a small fraction remaining as dissolved silica in the pore water ($f_{diss}Si$ = 0.5±0.4%). In contrast, Ge is almost exclusively removed by neoforming clays ($f_{sec}Ge$ = 91 ± 9%), with only a small portion taken up by vegetation ($f_{bio}Ge$ = 9 ± 9%) and even smaller fraction remaining in solution ($f_{diss}Ge$ = 0.2 ± 0.2%).

4.3.2 Importance of Si cycling by vegetation

It is important to preface the following discussion by noting that the partitioning of Ge and Si between neoforming clays and vegetation uptake is strongly dependent on the measured $\delta^{30}Si$ composition of just two vegetation samples, which may not be representative of the average local vegetation composition. However, 1) the sampled plants were selected to represent different types (a shrub and a grass) and were visually abundant in the studied area; 2) their measured $\delta^{30}Si$ compositions were very similar to each other (Table 1); 3) and the calculated vegetation fractionation factor ($\Delta^{30}Si_{bio-diss}$ = −1.0 ± 0.5‰) is highly consistent with previous studies (Frings et al., 2016).

Keeping the small sample size in mind, it is notable that our model results indicate that $f_{bio}Si$ is ~70 times higher than $f_{diss}Si$. A very similar result is obtained if using the Taconazo stream data to obtain a mass balance on a catchment-scale (Supp. Table S5). Therefore, the majority of labile (or bioavailable) Si is exported from the system as phytoliths, rather than as dissolved silica. This implies that the actual current chemical weathering flux of Si is many times higher than that which would be inferred from stream or pore water dissolved Si concentrations. Importantly, we are only modeling a "snapshot" of the current Si balance, and the model is agnostic to the ultimate long-term fate of the Si taken up by vegetation. In other words, the model predicts a significant net uptake of Si into phytoliths over the timescales over which porewaters and streams attain their signatures (likely on the order of days). However, it does not distinguish whether these phytoliths are being exported from the catchment (e.g., as leaf litter) or actively accumulating in the live vegetation or the soils, which would indicate a recent perturbation of the ecosystem. Although the immediate areas surrounding the sampled soil pits are classed as primary old-growth forest, some parts of the La Selva Biological station had been logged or agricultured to various degrees in the past (https://tropicalstudies.org, retrieved on 2019-07-30). It is therefore possible the high $f_{bio}Si$ calculated here does not represent a steady state and that live vegetation or soils are actively accumulating phytoliths due to relatively recent anthropogenic perturbations.

Overall, our results highlight the important role biocycling plays in the Si cycle at La Selva, consistent with findings in some other tropical ecosystems (Lucas et al., 1993b; Alexandre et al., 1997; Meunier et al., 1999) and supporting the hypothesis that Si overturn by terrestrial vegetation exerts major influence on the global Si cycle (Conley, 2002; Street-Perrott & Barker, 2008; Struyf et al., 2010; Cornelis & Delvaux, 2016). Furthermore, given the almost complete depletion of major cations (Table S1, Fig. S1), Si is the main chemical weathering product in La Selva soils. As a result, the biological uptake of Si may be considerably enhancing the chemical weathering rate of these soils, as dissolved Si uptake by plants in deeper soil horizons could lead to destabilization and enhanced dissolution of remaining silicate minerals. On the other hand, phytolith accumulation in upper soils, known as the biological pumping effect (Lucas et al., 1993a; Lucas, 2001), stabilizes silicate minerals in the topsoil, and has been used to explain the higher abundance of kaolinite in the topsoils of La Selva (Kleber et al., 2007), which may to some degree offset the enhanced weathering.

In summary, the use of Si isotopes and Ge/Si ratios has enabled us to quantify the fate of Si and Ge released via chemical weathering into the proportions that end up either exported in the dissolved phase or sequestered in neoforming clays or plant phytoliths. A more traditional approach would require an extensive sampling campaign to quantify these Si pools and their fluxes. Our simple proxy-based approach allows a first-order estimate of Si and Ge cycle dynamics and can be applied on a range of spatial scales (Baronas et al., 2018). Unavoidably, a number of assumptions underlie this approach and the results will be sensitive to how

well the isotopic or elemental composition of the different pools is represented by sparse sampling. However, all geochemical surveys of natural systems face a similar issue. In fact, in cases where the isotopic composition appears much less variable than the concentration of the element of interest (as is the case with Si in vegetation here: our two plant samples contain very different Si amounts but very similar $\delta^{30}Si_{veg}$ values; Table 1), the isotopic mass budget approach may offer much better precision.

4.4 Ge and Si as tracers of extreme weathering in volcanic soils

Understanding how the Ge and Si composition of soils and clays integrates different weathering processes over the long-term could be of particular value in weathering reconstructions using detrital paleorecords, where the degree of weathering cannot be assessed using conventional chemical alteration indices due to the absence of any parent material. Preferential retention of Ge and light Si isotopes in solid products of chemical weathering results in progressively higher Ge/Si and lower $\delta^{30}Si$ compositions with increasing weathering intensity (e.g., Kurtz et al., 2002; Opfergelt & Delmelle, 2012; Cornelis et al., 2014, 2019). Our results show that $\delta^{74}Ge$ signatures behave similarly, with the soils studied here representing the extreme end of this trend, with some of the lowest $\delta^{30}Si$ and $\delta^{74}Ge$ values measured to date (c.f. Frings et al., 2016; Qi et al., 2019). To better understand how Si and Ge isotopic signatures are related to chemical weathering, we first quantify the degree of gain or loss of elements during this process. We employ the widely used method of Brimhall and Dietrich (1987) and Chadwick et al. (1990), normalizing the element of interest X to a chemically immobile element (titanium in this case) in the sample of interest relative to the parent bedrock:

$$\tau_X = \frac{(X/Ti)_{sample}}{(X/Ti)_{bedrock}} - 1 \quad (4)$$

$\tau_X = 0$ when there is no loss or gain of X, whereas positive values indicate enrichment and negative values indicate depletion, with $\tau_X = -1$ indicating complete loss of X through chemical weathering. Zirconium and thorium were also evaluated as potential candidates for the immobile element to normalize against; however, Ti was chosen because it had a very similar concentrations in the two samples of parent material, whereas Zr and Th concentrations were variable (Table 1).

The results show that ~80% of Si and ~100% of alkali and alkaline earth elements have been lost through chemical weathering of La Selva soils (Table S1, Fig. S2). In contrast, the more immobile Fe and Al have been sightly enriched by 2-30%. Ge shows a lower degree of depletion (~20-40%) relative to Si, consistent with previously documented retention of Ge in secondary weathering products, such as aluminosilicates and Fe oxides (Murnane & Stallard, 1990; Kurtz et al., 2002). Finally, there does not appear to be any significant variation in chemical depletion with depth (Fig. S2), indicating that these soils have been extensively chemically weathered in the top 2 m and that the regolith-bedrock interface is likely to be found at much higher depths.

To assess more broadly how chemical weathering processes are reflected in soil and clay Ge/Si, $\delta^{30}Si$, and $\delta^{74}Ge$ signatures, we have compared our data with a compilation of previously published values for other volcanic soils in tropical areas (Fig. 5). The positive correlation between $\delta^{30}Si$ and τ_{Si} indicates that soil Si isotopes to a first order reflect the degree of Si loss from soils in a relatively linear fashion, reaching a maximum depletion between -2 and -3‰ as τ_{Si} approaches -1 (Fig. 5e). However, the lighter values of clays compared to bulk soils at La Selva demonstrate that additional Si isotopic fractionation can also take place without elemental Si depletion.

Similarly, $\delta^{74}Ge$ shows strong linear correlation with τ_{Ge} (Fig. 5a), consistent with the loss of isotopically heavy dissolved Ge (this study, Baronas et al., 2017, 2018). In contrast to $\delta^{30}Si$, neoformed clay $\delta^{74}Ge$ signatures are indistinguishable from bulk soil, which is consis-

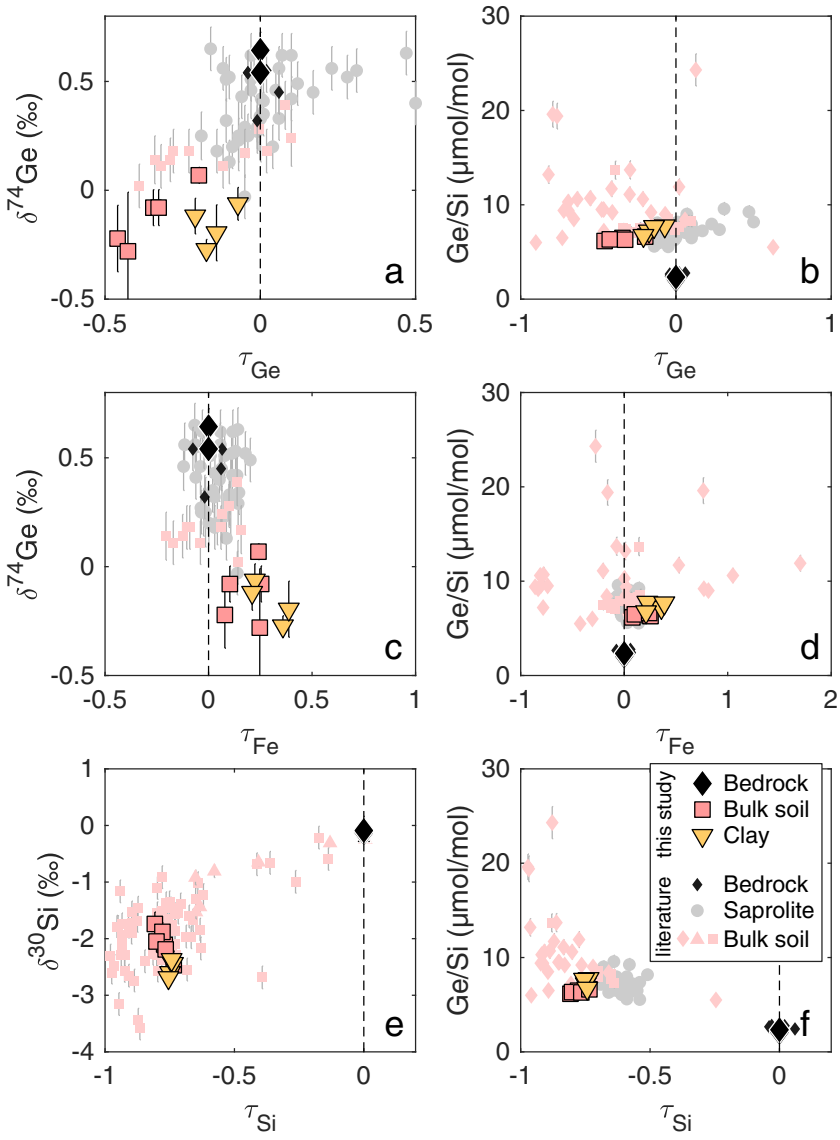

Figure 5. Relationships between δ^{74}Ge, δ^{30}Si, and Ge/Si vs. fractional elemental loss of Ge, Fe, and Si (Eq. 4) in volcanic soils. Small symbols are published values of Kurtz et al. (2002) (Ge/Si; diamonds) and Bern et al. (2010) (δ^{30}Si corrected for dust inputs; squares) for basaltic soils in Hawaii, Qi et al. (2019) for a basaltic weathering profile in Hainan island, China (δ^{74}Ge and Ge/Si; squares and circles), and Opfergelt et al. (2012) for an andesitic soil sequence in Guadeloupe island, French Indies (δ^{30}Si; triangles).

tent with the fact that almost all Ge released during chemical weathering is retained in these phases ($f_{sec}Ge = 91 \pm 9\%$, see Section 4.3.1). Similar distinction between Ge and Si behavior was already noted using the dissolved and suspended sediment composition of Peruvian rivers (Baronas et al., 2018). As a result, even though both elements exhibit fractionation factors of similar magnitude, secondary weathering phases are significantly less fractionated with regards to δ^{74}Ge. Germanium can exhibit siderophile behavior, and incorporation of Ge into Fe oxides can result in isotopic fractionation in the laboratory (Pokrovsky et al., 2014), in marine sediments (Baronas et al., 2019), and potentially during continental weathering (Baronas et al., 2018). While lower δ^{74}Ge values appear to be associated with slightly higher τ_{Fe} in volcanic soils, this relationship is too weak to suggest a mechanistic control of δ^{74}Ge by Fe oxides (Fig. 5c). Similarly, Kurtz et al. (2002) have noted that Fe does not appear to control Ge/Si fractionation in Hawaiian soils, which is further supported by additional data in this and other recent studies (Fig. 5d). Instead, it appears that Ge/Si fractionation in volcanic soils is primarily driven by the preferential loss of Si, rather than the enrichment of Ge (Fig. 5b,f).

These findings have important implications for the potential use of Si and Ge isotopes as tracers of chemical weathering intensity in detrital paleorecords. Due to the high affinity of Ge to secondary phases, δ^{74}Ge composition of detrital material will be less sensitive to weathering compared to δ^{30}Si. Based on the Ge isotope dynamics established here, we would expect to find significantly lighter δ^{74}Ge, below -0.5 ‰, only in even more extremely weathered soils than those studied here, such as those developed on the oldest Hawaiian island Kauai, which have been shown to exhibit τ_{Ge} close to -1 (Kurtz et al., 2002). If this hypothesis is correct, detrital δ^{74}Ge records could conceivably help reconstruct weathering intensity during some of the hottest periods in Earth's history, such as the early Eocene (Zachos et al., 2001), further improving our understanding of the links between tectonics, weathering, and climate.

5 Conclusions

In this study we used the distribution of Ge/Si and Ge and Si isotope ratios in the tropical forest soils and waters of La Selva Biological Station, Costa Rica (Fig. 1), to better understand the biogeochemical cycling of these elements during the intense weathering of volcanic rocks. The studied soils are depleted of major cations and composed almost entirely of secondary aluminosilicate and oxide phases which are uniformly enriched in Ge/Si and light Ge and Si isotopes relative to the parent bedrock (Fig. 2). The chemical and isotopic composition of investigated streams is highly variable and derives from the mixing of two distinct types of fluids (Fig. 3): 1) local soil waters reflecting weathering of the depleted lowland soils; and 2) solute-rich interbasin groundwater (IBGW) derived from higher elevations and reflecting the weathering of fresh volcanic rock, as observed by previous researchers (e.g., Pringle, 1991; Genereux et al., 2009). In both cases, weathering produces fluids that have higher δ^{74}Ge and δ^{30}Si and lower Ge/Si than the weathering source substrate, consistent with previous studies on Ge and Si fractionation. The derived fractionation factors were similar in both environments: $\Delta^{30}Si_{sec-diss} = -1.2 \pm 0.1$‰ and -1.7 ± 0.5‰ for the weathering of volcanic rock by IBGW and for the weathering of lowland soils, respectively. The equivalent Ge isotope fractionation factors were $\Delta^{74}Ge_{sec-diss} = -3.0 \pm 0.9$‰ for IBGW and -2.3 ± 0.2‰ for lowland soils. Reactive transport modeling suggests that IBGW fluids have likely reached chemical and isotopic equilibrium with volcanic rock and precipitating secondary phases. It is notable that the Si and Ge isotope fractionation factors appear to remain relatively constant even in extremely weathered systems, with an isotopic shift of all reservoirs driven by a continuous loss of heavier isotopes in dissolved form. The measured Ge and Si isotope signatures and fractionation factors are summarized in Supp. Fig. S6.

We used a simple mass balance modeling approach (Baronas et al., 2018) to show that 91±9% of Ge released via chemical weathering of lowland soils is sequestered by neoforming Al-Si-Fe clays, 9±9% is taken up by vegetation, and only 0.2±0.2% remains dissolved in the soil pore waters. In contrast, 61±14% of Si is sequestered by neoforming clays, 39± 14% by vegetation, and 0.5 ± 0.4% remains as dissolved silica (Fig. 4). Similar results are

obtained applying the model on a catchment scale (assuming that our soil samples are representative across the Taconazo catchment). This may indicate that Si is being actively accumulated in plant phytoliths, either in the soils or in standing vegetation, as secondary forest of previously cleared areas matures. These results highlight the important role that biological Si cycling can play in tropical ecosystems sustained by highly weathered soils.

Finally, we compiled a number of previous studies of tropical volcanic soils (Kurtz et al., 2002; Bern et al., 2010; Opfergelt et al., 2012; Qi et al., 2019) to identify the first order controls on δ^{74}Ge, δ^{30}Si, and Ge/Si signatures in solid weathering products (Fig. 5). We show that globally, soil δ^{74}Ge closely tracks the depletion of Ge by chemical weathering (τ_{Ge}), whereas δ^{30}Si and Ge/Si both reflect the loss of Si (τ_{Si}). Because Ge is more efficiently retained in solid weathering products than Si, and because Ge and Si isotope signatures reflect the relative mobility of each element, a δ^{74}Ge-δ^{30}Si multi-proxy system is sensitive to a wider range of weathering intensities than each isotopic system in isolation. In particular, we hypothesize that solid weathering products with δ^{74}Ge < -0.5 ‰ could be indicative of extremely high weathering intensity environments, where hot and humid conditions are combined with very limited erosion.

References

Abraham, K., Opfergelt, S., Fripiat, F., Cavagna, A. J., de Jong, J. T., Foley, S. F., ... Cardinal, D. (2008). δ30Si and δM29Si Determinations on USGS BHVO-1 and BHVO-2 Reference Materials with a New Configuration on a Nu Plasma Multi-Collector ICP-MS. *Geostandards and Geoanalytical Research*, *32*(2), 193–202. doi: 10.1111/j.1751-908X.2008.00879.x

Alexandre, A., Meunier, J.-D., Colin, F., & Koud, J.-M. (1997). Plant impact on the biogeochemical cycle of silicon and related weathering processes. *Geochimica et Cosmochimica Acta*, *61*(3), 677–682.

Alvarado Induni, G. E. (1990). Caracteristicas geologicas de la Estacion Biologica La Selva. *Tecnologia en Marcha*, *10*(3), 11–22.

Amundson, R. (2013). Soil Formation. In *Treatise on geochemistry: Second edition* (2nd ed., Vol. 7, pp. 1–26). Elsevier Ltd. Retrieved from http://dx.doi.org/10.1016/B978-0-08-095975-7.00501-5 doi: 10.1016/B978-0-08-095975-7.00501-5

Anders, A. M., Sletten, R., Derry, L., & Hallet, B. (2003). Germanium/silicon ratios in the Copper River Basin, Alaska: Weathering and partitioning in periglacial versus glacial environments. *Journal of Geophysical Research*, *108*(F1), 6005. Retrieved from http://www.agu.org/pubs/crossref/2003/2003JF000026.shtml doi: 10.1029/2003JF000026

Baronas, J. J., Hammond, D. E., Berelson, W. M., McManus, J., & Severmann, S. (2016). Germanium-silicon fractionation in a river-influenced continental margin: The Northern Gulf of Mexico. *Geochimica et Cosmochimica Acta*, *178*, 124–142. Retrieved from http://linkinghub.elsevier.com/retrieve/pii/S0016703716300126 doi: 10.1016/j.gca.2016.01.028

Baronas, J. J., Hammond, D. E., McManus, J., Wheat, C. G., & Siebert, C. (2017, 4). A global Ge isotope budget. *Geochimica et Cosmochimica Acta*, *203*, 265–283. Retrieved from http://linkinghub.elsevier.com/retrieve/pii/S0016703717300121 doi: 10.1016/j.gca.2017.01.008

Baronas, J. J., Hammond, D. E., Rouxel, O. J., & Monteverde, D. R. (2019). A first look at dissolved Ge isotopes in marine sediments. *Frontiers in Earth Science*, *7*(June), 1–17. doi: 10.3389/feart.2019.00162

Baronas, J. J., Torres, M. A., West, A. J., Rouxel, O. J., Georg, R. B., Bouchez, J., ... Hammond, D. E. (2018, 12). Ge and Si isotope signatures in rivers: A quantitative multi-proxy approach. *Earth and Planetary Science Letters*, *503*, 194–215. Retrieved from https://linkinghub.elsevier.com/retrieve/pii/S0012821X18305612 doi: 10.1016/j.epsl.2018.09.022

Bern, C. R., Brzezinski, M. a., Beucher, C., Ziegler, K., & Chadwick, O. a. (2010, 2). Weathering, dust, and biocycling effects on soil silicon isotope ratios. *Geochimica et Cosmochimica Acta*, *74*(3), 876–889. Retrieved from http://linkinghub.elsevier.com/retrieve/pii/S0016703709006851https://linkinghub.elsevier.com/retrieve/pii/S0016703709006851 doi: 10.1016/j.gca.2009.10.046

Berner, R., Lasaga, A., & Garrels, R. (1983). The carbonate-silicate geochemical cycle and its effect on atmospheric carbon dioxide over the past 100 million years. *American Journal of Science*, *283*, 641–683. Retrieved from http://shadow.eas.gatech.edu/~jean/paleo/Berner_1983.pdf

Bernstein, L. (1985). Germanium geochemistry and mineralogy. *Geochimica et Cosmochimica Acta*, *49*, 2409–2422. Retrieved from http://www.sciencedirect.com/science/article/pii/0016703785902418

Blanchard, M., Balan, E., & Schauble, E. A. (2017, 1). Equilibrium Fractionation of Non-traditional Isotopes: a Molecular Modeling Perspective. *Reviews in Mineralogy and Geochemistry*, *82*(1), 27–63. Retrieved from http://rimg.geoscienceworld.org/lookup/doi/10.2138/rmg.2017.82.2 doi: 10.2138/rmg.2017.82.2

Blecker, S. W., King, S. L., Derry, L. A., Chadwick, O. A., Ippolito, J. A., & Kelly, E. F. (2007, 8). The ratio of germanium to silicon in plant phytoliths: Quantification of

biological discrimination under controlled experimental conditions. *Biogeochemistry*, *86*(2), 189–199. Retrieved from http://www.springerlink.com/index/10.1007/s10533-007-9154-7 doi: 10.1007/s10533-007-9154-7

Bouchez, J., von Blanckenburg, F., & Schuessler, J. A. (2013, 4). Modeling novel stable isotope ratios in the weathering zone. *American Journal of Science*, *313*(4), 267–308. Retrieved from http://www.ajsonline.org/cgi/doi/10.2475/04.2013.01 doi: 10.2475/04.2013.01

Brantley, S., Kubicki, J., & White, A. (2008). *Kinetics of water-rock interaction* (S. Brantley, J. Kubicki, & A. White, Eds.). New York: Springer. Retrieved from http://link.springer.com/content/pdf/10.1007/978-0-387-73563-4.pdf

Brimhall, G. H., & Dietrich, W. E. (1987). Constitutive mass balance relations between chemical composition, volume, density, porosity, and strain in metasomatic hydrochemical systems: Results on weathering and pedogenesis. *Geochimica et Cosmochimica Acta*, *51*(3), 567–587.

Chadwick, O. A., Brimhall, G. H., & Hendricks, D. M. (1990). From a black to a gray box - a mass balance interpretation of pedogenesis. *Geomorphology*, *3*(3-4), 369–390. doi: 10.1016/0169-555X(90)90012-F

Clark, D., & Clark, D. (2000). Landscape-scale variation in forest structure and biomass in a tropical rain forest. *Forest Ecology and Management*, *137*(1-3), 185–198. Retrieved from http://www.sciencedirect.com/science/article/pii/S0378112799003278 doi: 10.1016/S0378-1127(99)00327-8

Conley, D. J. (2002). Terrestrial ecosystems and the global biogeochemical silica cycle. *Global Biogeochemical Cycles*, *16*(4), 1–8. Retrieved from http://www.agu.org/pubs/crossref/2002/2002GB001894.shtml doi: 10.1029/2002GB001894

Cornelis, J.-T., & Delvaux, B. (2016, 8). Soil processes drive the biological silicon feedback loop. *Functional Ecology*, *30*(8), 1298–1310. Retrieved from http://doi.wiley.com/10.1111/1365-2435.12704 doi: 10.1111/1365-2435.12704

Cornelis, J.-T., Delvaux, B., Cardinal, D., André, L., Ranger, J., & Opfergelt, S. (2010, 7). Tracing mechanisms controlling the release of dissolved silicon in forest soil solutions using Si isotopes and Ge/Si ratios. *Geochimica et Cosmochimica Acta*, *74*(14), 3913–3924. Retrieved from http://linkinghub.elsevier.com/retrieve/pii/S0016703710002413 doi: 10.1016/j.gca.2010.04.056

Cornelis, J.-T., Weis, D., Lavkulich, L., Vermeire, M.-L., Delvaux, B., & Barling, J. (2014, 12). Silicon isotopes record dissolution and re-precipitation of pedogenic clay minerals in a podzolic soil chronosequence. *Geoderma*, *235-236*, 19–29. Retrieved from http://linkinghub.elsevier.com/retrieve/pii/S0016706114002535 doi: 10.1016/j.geoderma.2014.06.023

Cornelis, J.-T., Weis, D., Opfergelt, S., Van Ranst, E., & Dumon, M. (2019, 10). Past and current geochemical conditions influence silicon isotope signatures of pedogenic clay minerals at the soil profile scale, Ethiopia. *Chemical Geology*, *524*(June), 174–183. Retrieved from https://doi.org/10.1016/j.chemgeo.2019.06.013https://linkinghub.elsevier.com/retrieve/pii/S0009254119303080 doi: 10.1016/j.chemgeo.2019.06.013

De Argollo, R., & Schilling, J.-G. (1978, 6). Ge-Si and Ga-Al fractionation in Hawaiian volcanic rocks. *Geochimica et Cosmochimica Acta*, *42*(6), 623–630. Retrieved from http://linkinghub.elsevier.com/retrieve/pii/0016703778900078 doi: 10.1016/0016-7037(78)90007-8

Dellinger, M., Gaillardet, J., Bouchez, J., Calmels, D., Louvat, P., Dosseto, A., . . . Maurice, L. (2015). Riverine Li isotope fractionation in the Amazon River basin controlled by the weathering regimes. *Geochimica et Cosmochimica Acta*, *164*, 71–93. Retrieved from http://linkinghub.elsevier.com/retrieve/pii/S0016703715002483 doi: 10.1016/j.gca.2015.04.042

Delstanche, S., Opfergelt, S., Cardinal, D., Elsass, F., André, L., & Delvaux, B. (2009, 2). Silicon isotopic fractionation during adsorption of aqueous monosilicic acid onto iron oxide. *Geochimica et Cosmochimica Acta*, *73*(4), 923–934. Retrieved from

http://linkinghub.elsevier.com/retrieve/pii/S0016703708006832 doi: 10.1016/j.gca.2008.11.014

Delvigne, C., Opfergelt, S., Cardinal, D., Delvaux, B., & André, L. (2009, 5). Distinct silicon and germanium pathways in the soil-plant system: Evidence from banana and horsetail. *Journal of Geophysical Research*, *114*(G2), G02013. Retrieved from http://www.agu.org/pubs/crossref/2009/2008JG000899.shtml doi: 10.1029/2008JG000899

Derry, L. A., Kurtz, A. C., Ziegler, K., & Chadwick, O. A. (2005, 2). Biological control of terrestrial silica cycling and export fluxes to watersheds. *Nature*, *433*, 728–31. Retrieved from http://www.ncbi.nlm.nih.gov/pubmed/15716949 doi: 10.1038/nature03299

Ding, T., Ma, G., Shui, M., Wan, D., & Li, R. (2005, 5). Silicon isotope study on rice plants from the Zhejiang province, China. *Chemical Geology*, *218*(1-2), 41–50. Retrieved from http://linkinghub.elsevier.com/retrieve/pii/S0009254105000823 doi: 10.1016/j.chemgeo.2005.01.018

Escoube, R., Rouxel, O. J., Edwards, K., Glazer, B., & Donard, O. F. X. (2015). Coupled Ge/Si and Ge isotope ratios as geochemical tracers of seafloor hydrothermal systems: Case studies at Loihi Seamount and East Pacific Rise 9°50'N. *Geochimica et Cosmochimica Acta*, *167*, 93–112. Retrieved from http://linkinghub.elsevier.com/retrieve/pii/S0016703715004081 doi: 10.1016/j.gca.2015.06.025

Escoube, R., Rouxel, O. J., Luais, B., Ponzevera, E., & Donard, O. F. (2012, 6). An Intercomparison Study of the Germanium Isotope Composition of Geological Reference Materials. *Geostandards and Geoanalytical Research*, *36*(2), 149–159. Retrieved from http://doi.wiley.com/10.1111/j.1751-908X.2011.00135.x doi: 10.1111/j.1751-908X.2011.00135.x

Fernandez, N. M., Zhang, X., & Druhan, J. L. (2019). Silicon isotopic re-equilibration during amorphous silica precipitation and implications for isotopic signatures in geochemical proxies. *Geochimica et Cosmochimica Acta*. Retrieved from https://linkinghub.elsevier.com/retrieve/pii/S0016703719304533 doi: 10.1016/j.gca.2019.07.029

Frings, P. J., & Buss, H. L. (2019). The Central Role of Weathering in the Geosciences. *Elements*, *15*(4), 229–234. Retrieved from https://pubs.geoscienceworld.org/msa/elements/article/15/4/229/572792/The-Central-Role-of-Weathering-in-the-Geosciences doi: 10.2138/gselements.15.4.229

Frings, P. J., Clymans, W., Fontorbe, G., De La Rocha, C. L., & Conley, D. J. (2016, 5). The continental Si cycle and its impact on the ocean Si isotope budget. *Chemical Geology*, *425*, 12–36. Retrieved from http://dx.doi.org/10.1016/j.chemgeo.2016.01.020http://linkinghub.elsevier.com/retrieve/pii/S0009254116300201 doi: 10.1016/j.chemgeo.2016.01.020

Froelich, P., Blanc, V., Mortlock, R., Chillrud, S., Dunstan, W., Udomkit, A., & Peng, T. (1992). River fluxes of dissolved silica to the ocean were higher during glacials: Ge/Si in diatoms, rivers, and oceans. *Paleoceanography*, *7*(6), 739–767. Retrieved from http://www.agu.org/pubs/crossref/1992.../92PA02090.shtml

Froelich, P., Hambrick, G., Andreae, M., Mortlock, R., & Edmond, J. (1985). The geochemistry of inorganic germanium in natural waters. *Journal of Geophysical Research*, *90*(C1), 1133–1141. Retrieved from http://onlinelibrary.wiley.com/doi/10.1029/JC090iC01p01133/full

Genereux, D. P., & Jordan, M. (2006, 4). Interbasin groundwater flow and groundwater interaction with surface water in a lowland rainforest, Costa Rica: A review. *Journal of Hydrology*, *320*(3-4), 385–399. Retrieved from http://linkinghub.elsevier.com/retrieve/pii/S0022169405003574 doi: 10.1016/j.jhydrol.2005.07.023

Genereux, D. P., Jordan, M. T., & Carbonell, D. (2005). A paired-watershed budget study to quantify interbasin groundwater flow in a lowland rain forest, Costa Rica. *Water Resources Research*, *41*, 1–17. doi: 10.1029/2004WR003635

Genereux, D. P., Webb, M., & Solomon, D. K. (2009, 8). Chemical and isotopic signature

of old groundwater and magmatic solutes in a Costa Rican rain forest: Evidence from carbon, helium, and chlorine. *Water Resources Research*, *45*(8). Retrieved from http://doi.wiley.com/10.1029/2008WR007630 doi: 10.1029/2008WR007630

Genereux, D. P., Wood, S. J., & Pringle, C. M. (2002). Chemical tracing of interbasin groundwater transfer in the lowlandrainforest of Costa Rica. *Journal of Hydrology*, *258*, 163–178. doi: 10.1016/S0022-1694(01)00568-6

Georg, R., Reynolds, B., Frank, M., & Halliday, A. (2006a, 9). Mechanisms controlling the silicon isotopic compositions of river waters. *Earth and Planetary Science Letters*, *249*(3-4), 290–306. Retrieved from http://dx.doi.org/10.1016/j.epsl.2006.07.006 doi: 10.1016/j.epsl.2006.07.006

Georg, R., Reynolds, B., Frank, M., & Halliday, A. (2006b, 11). New sample preparation techniques for the determination of Si isotopic compositions using MC-ICPMS. *Chemical Geology*, *235*(1-2), 95–104. Retrieved from http://linkinghub.elsevier.com/retrieve/pii/S000925410600307X doi: 10.1016/j.chemgeo.2006.06.006

Georg, R., Reynolds, B., West, A., Burton, K., & Halliday, A. (2007, 9). Silicon isotope variations accompanying basalt weathering in Iceland. *Earth and Planetary Science Letters*, *261*(3-4), 476–490. Retrieved from http://linkinghub.elsevier.com/retrieve/pii/S0012821X07004530 doi: 10.1016/j.epsl.2007.07.004

Georg, R., West, A., Basu, A. R., & Halliday, A. N. (2009, 6). Silicon fluxes and isotope composition of direct groundwater discharge into the Bay of Bengal and the effect on the global ocean silicon isotope budget. *Earth and Planetary Science Letters*, *283*(1-4), 67–74. Retrieved from http://linkinghub.elsevier.com/retrieve/pii/S0012821X09002003 doi: 10.1016/j.epsl.2009.03.041

Georg, R., Zhu, C., Reynolds, B., & Halliday, A. (2009, 4). Stable silicon isotopes of groundwater, feldspars, and clay coatings in the Navajo Sandstone aquifer, Black Mesa, Arizona, USA. *Geochimica et Cosmochimica Acta*, *73*(8), 2229–2241. Retrieved from http://linkinghub.elsevier.com/retrieve/pii/S0016703709000726 doi: 10.1016/j.gca.2009.02.005

Guillermic, M., Lalonde, S. V., Hendry, K. R., & Rouxel, O. J. (2017). The isotope composition of inorganic germanium in seawater and deep sea sponges. *Geochimica et Cosmochimica Acta*, *212*, 99–118. Retrieved from http://dx.doi.org/10.1016/j.gca.2017.06.011 doi: 10.1016/j.gca.2017.06.011

Hammond, D. E., McManus, J., & Berelson, W. M. (2004). Oceanic germanium/silicon ratios: Evaluation of the potential overprint of temperature on weathering signals. *Paleoceanography*, *19*, PA2016. Retrieved from http://www.agu.org/pubs/crossref/2004/2003PA000940.shtml doi: 10.1029/2003PA000940

Hathorne, E. C., & James, R. H. (2006). Temporal record of lithium in seawater: A tracer for silicate weathering? *Earth and Planetary Science Letters*, *246*(3-4), 393–406. doi: 10.1016/j.epsl.2006.04.020

Hughes, H., Sondag, F., Santos, R., André, L., & Cardinal, D. (2013, 11). The riverine silicon isotope composition of the Amazon Basin. *Geochimica et Cosmochimica Acta*, *121*, 637–651. Retrieved from http://linkinghub.elsevier.com/retrieve/pii/S0016703713004304 doi: 10.1016/j.gca.2013.07.040

Johnson, C. M., Beard, B. L., & Albarede, F. (2004). Overview and General Concepts. *Reviews in Mineralogy and Geochemistry*, *55*(1), 1–24. doi: 10.2138/gsrmg.55.1.1

Kautz, C. Q., & Ryan, P. C. (2003). The 10 A to 7 A halloysite transition in a tropical soil sequence, Costa Rica. *Clays and Clay Minerals*, *51*(3), 252–263. doi: 10.1346/CCMN.2003.0510302

Kleber, M., Schwendenmann, L., Veldkamp, E., Rößner, J., & Jahn, R. (2007, 2). Halloysite versus gibbsite: Silicon cycling as a pedogenetic process in two lowland neotropical rain forest soils of La Selva, Costa Rica. *Geoderma*, *138*(1-2), 1–11. Retrieved from http://linkinghub.elsevier.com/retrieve/pii/S0016706106002904 doi: 10.1016/j.geoderma.2006.10.004

Kurtz, A., Derry, L., & Chadwick, O. (2002). Germanium-silicon fractionation in the

weathering environment. *Geochimica et Cosmochimica Acta*, *66*(9), 1525–1537. Retrieved from http://www.sciencedirect.com/science/article/pii/S0016703701008699

Li, G., & Elderfield, H. (2013, 2). Evolution of carbon cycle over the past 100 million years. *Geochimica et Cosmochimica Acta*, *103*, 11–25. Retrieved from http://linkinghub.elsevier.com/retrieve/pii/S001670371200590X doi: 10.1016/j.gca.2012.10.014

Li, G., & West, A. J. (2014, 9). Evolution of Cenozoic seawater lithium isotopes: Coupling of global denudation regime and shifting seawater sinks. *Earth and Planetary Science Letters*, *401*, 284–293. Retrieved from http://linkinghub.elsevier.com/retrieve/pii/S0012821X14003884 doi: 10.1016/j.epsl.2014.06.011

Lucas, Y. (2001, 5). The Role of Plants in Controlling Rates and Products of Weathering: Importance of Biological Pumping. *Annual Review of Earth and Planetary Sciences*, *29*(1), 135–163. Retrieved from http://www.annualreviews.org/doi/10.1146/annurev.earth.29.1.135 doi: 10.1146/annurev.earth.29.1.135

Lucas, Y., Luizao, F. J., Chauvel, A., Rouiller, J., & Nahon, D. (1993a). The relation between biological activity of the rain forest and mineral composition of soils. *Science*, *260*(5107), 521–523. doi: 10.1126/science.260.5107.521

Lucas, Y., Luizao, F. J., Chauvel, A., Rouiller, J., & Nahon, D. (1993b, 4). The Relation Between Biological Activity of the Rain Forest and Mineral Composition of Soils. *Science*, *260*(5107), 521–523. Retrieved from http://www.sciencemag.org/cgi/doi/10.1126/science.260.5107.521 doi: 10.1126/science.260.5107.521

Lugolobi, F., Kurtz, A. C., & Derry, L. A. (2010, 2). Germanium-silicon fractionation in a tropical, granitic weathering environment. *Geochimica et Cosmochimica Acta*, *74*(4), 1294–1308. Retrieved from http://linkinghub.elsevier.com/retrieve/pii/S0016703709007261 doi: 10.1016/j.gca.2009.11.027

Macdonald, F. A., Swanson-Hysell, N. L., Park, Y., Lisiecki, L., & Jagoutz, O. (2019). Arc-continent collisions in the tropics set Earth's climate state. *Science*, *5300*(March), 1–12.

Maher, K., & Chamberlain, C. P. (2014, 3). Hydrologic regulation of chemical weathering and the geologic carbon cycle. *Science*, *343*(6178), 1502–4. Retrieved from http://science.sciencemag.org/content/343/6178/1502.long doi: 10.1126/science.1250770

McDade, L. A., Bawa, K. S., Hespenheide, H. A., & Hartshorn, G. S. (1994). *La Selva: Ecology and Natural History of a Neotropical Rain Forest*. University of Chicago Press.

Meek, K., Derry, L., Sparks, J., & Cathles, L. (2016, 4). 87Sr/86Sr, Ca/Sr, and Ge/Si ratios as tracers of solute sources and biogeochemical cycling at a temperate forested shale catchment, central Pennsylvania, USA. *Chemical Geology*. Retrieved from http://linkinghub.elsevier.com/retrieve/pii/S0009254116302078 doi: 10.1016/j.chemgeo.2016.04.026

Meunier, J. D., Colin, F., & Alarcon, C. (1999). Biogenic silica storage in soils. *Geology*, *27*(9), 835–838.

Misra, S., & Froelich, P. N. (2012, 2). Lithium isotope history of Cenozoic seawater: changes in silicate weathering and reverse weathering. *Science*, *335*(6070), 818–823. Retrieved from http://science.sciencemag.org/content/335/6070/818.long doi: 10.1126/science.1214697

Mortlock, R., & Froelich, P. (1987). Continental weathering of germanium: Ge/Si in the global river discharge. *Geochimica et Cosmochimica Acta*, *51*, 2075–2082. Retrieved from http://www.sciencedirect.com/science/article/pii/0016703787902572

Mortlock, R., & Froelich, P. (1996). Determination of germanium by isotope dilution-hydride generation inductively coupled plasma mass spectrometry. *Analytica Chimica Acta*, *332*, 277–284. Retrieved from http://www.sciencedirect.com/science/article/pii/0003267096002309

Murnane, R., & Stallard, R. (1990). Germanium and silicon in rivers of the Orinoco drainage basin. *Nature*, *344*, 749–752. Retrieved from http://www.nature.com/nature/journal/v344/n6268/abs/344749a0.html

Oelze, M., von Blanckenburg, F., Bouchez, J., Hoellen, D., & Dietzel, M. (2015). The effect of Al on Si isotope fractionation investigated by silica precipitation experiments. *Chemical Geology*, *397*, 94–105. Retrieved from http://linkinghub.elsevier.com/retrieve/pii/S0009254115000078 doi: 10.1016/j.chemgeo.2015.01.002

Oelze, M., von Blanckenburg, F., Hoellen, D., Dietzel, M., & Bouchez, J. (2014). Si stable isotope fractionation during adsorption and the competition between kinetic and equilibrium isotope fractionation: Implications for weathering systems. *Chemical Geology*, *380*, 161–171. Retrieved from http://linkinghub.elsevier.com/retrieve/pii/S0009254114002265 doi: 10.1016/j.chemgeo.2014.04.027

Opfergelt, S., Cardinal, D., André, L., Delvigne, C., Bremond, L., & Delvaux, B. (2010, 1). Variations of δ30Si and Ge/Si with weathering and biogenic input in tropical basaltic ash soils under monoculture. *Geochimica et Cosmochimica Acta*, *74*(1), 225–240. Retrieved from http://linkinghub.elsevier.com/retrieve/pii/S0016703709006036 doi: 10.1016/j.gca.2009.09.025

Opfergelt, S., Cardinal, D., Henriet, C., Draye, X., André, L., & Delvaux, B. (2006, 6). Silicon Isotopic Fractionation by Banana (Musa spp.) Grown in a Continuous Nutrient Flow Device. *Plant and Soil*, *285*(1-2), 333–345. Retrieved from http://link.springer.com/10.1007/s11104-006-9019-1 doi: 10.1007/s11104-006-9019-1

Opfergelt, S., & Delmelle, P. (2012). Silicon isotopes and continental weathering processes: Assessing controls on Si transfer to the ocean. *Comptes Rendus - Geoscience*, *344*(11-12), 723–738. Retrieved from http://dx.doi.org/10.1016/j.crte.2012.09.006 doi: 10.1016/j.crte.2012.09.006

Opfergelt, S., Georg, R., Delvaux, B., Cabidoche, Y.-M., Burton, K., & Halliday, A. (2012, 10). Silicon isotopes and the tracing of desilication in volcanic soil weathering sequences, Guadeloupe. *Chemical Geology*, *326-327*, 113–122. Retrieved from http://linkinghub.elsevier.com/retrieve/pii/S0009254112003609 doi: 10.1016/j.chemgeo.2012.07.032

Pogge von Strandmann, P. A. E., & Henderson, G. M. (2015, 1). The Li isotope response to mountain uplift. *Geology*, *43*(1), 67–70. Retrieved from http://geology.gsapubs.org/cgi/doi/10.1130/G36162.1 doi: 10.1130/G36162.1

Pogge von Strandmann, P. A. E., Porcelli, D., James, R. H., van Calsteren, P., Schaefer, B., Cartwright, I., . . . Burton, K. W. (2014). Chemical weathering processes in the Great Artesian Basin: Evidence from lithium and silicon isotopes. *Earth and Planetary Science Letters*, *406*(0), 24–36. Retrieved from http://www.sciencedirect.com/science/article/pii/S0012821X1400569X doi: 10.1016/j.epsl.2014.09.014

Pokrovsky, O. S., Galy, A., Schott, J., Pokrovski, G. S., & Mantoura, S. (2014, 4). Germanium isotope fractionation during Ge adsorption on goethite and its coprecipitation with Fe oxy(hydr)oxides. *Geochimica et Cosmochimica Acta*, *131*, 138–149. Retrieved from http://linkinghub.elsevier.com/retrieve/pii/S0016703714000672 doi: 10.1016/j.gca.2014.01.023

Porcelli, D. (2008). Chapter 4 Investigating Groundwater Processes Using U- and Th-Series Nuclides. *Radioactivity in the Environment*, *13*(07), 105–153. doi: 10.1016/S1569-4860(07)00004-6

Pringle, C. (1991). Geothermally modified waters surface at La Selva Biological Station, Costa Rica: volcanic processes introduce chemical discontinuities into lowland tropical streams. *Biotropica*, *23*(4), 523–529. Retrieved from http://www.jstor.org/stable/2388390

Pringle, C., Triska, F., & Browder, G. (1990). Spatial variation in basic chemistry of streams draining a volcanic landscape on Costa Rica's Caribbean slope. *Hydrobiologia*, *206*, 73–85. Retrieved from http://link.springer.com/article/10.1007/BF00018971

Qi, H. W., Hu, R. Z., Jiang, K., Zhou, T., Liu, Y. F., & Xiong, Y. W. (2019). Germanium isotopes and Ge/Si fractionation under extreme tropical weathering of basalts from the Hainan Island, South China. *Geochimica et Cosmochimica Acta*, *253*, 249–266. Retrieved from https://doi.org/10.1016/j.gca.2019.03.022 doi: 10.1016/j.gca.2019.03.022

Raymo, M. E., & Ruddiman, W. F. (1992, 9). Tectonic forcing of late Cenozoic climate. *Nature*, *359*(6391), 117–122. Retrieved from http://www.meteo.mcgill.ca/~tremblay/Courses/ATOC183/Readings/RaymoRuddiman.Nature.1992.pdfhttp://www.nature.com/doifinder/10.1038/359117a0 doi: 10.1038/359117a0

Reynolds, B., Aggarwal, J., Brzezinski, M., Cardinal, D., Engstrom, E., Georg, R., ... Vroon, P. (2007). An inter-laboratory comparison of Si isotope reference materials. *Journal of Analytical Atomic Spectrometry*, *22*, 561–568. Retrieved from http://www.sciencedirect.com/science/journal/00167037 doi: 10.1039/b616755a

Roerdink, D. L., van den Boorn, S. H., Geilert, S., Vroon, P. Z., & van Bergen, M. J. (2015). Experimental constraints on kinetic and equilibrium silicon isotope fractionation during the formation of non-biogenic chert deposits. *Chemical Geology*, *402*, 40–51. Retrieved from http://linkinghub.elsevier.com/retrieve/pii/S0009254115001205 doi: 10.1016/j.chemgeo.2015.02.038

Rouxel, O. J., Galy, A., & Elderfield, H. (2006, 7). Germanium isotopic variations in igneous rocks and marine sediments. *Geochimica et Cosmochimica Acta*, *70*(13), 3387–3400. Retrieved from http://linkinghub.elsevier.com/retrieve/pii/S0016703706002250 doi: 10.1016/j.gca.2006.04.025

Rouxel, O. J., & Luais, B. (2017, 1). Germanium Isotope Geochemistry. *Reviews in Mineralogy and Geochemistry*, *82*(1), 601–656. Retrieved from http://rimg.geoscienceworld.org/lookup/doi/10.2138/rmg.2017.82.14 doi: 10.2138/rmg.2017.82.14

Sanford, R., Paaby, P., Luvall, J., & Phillips, E. (1994). Climate, Geomorphology, and Aquatic Systems. In *La selva: Ecology and natural history of a tropical rainforest* (pp. 19–33). University of Chicago Press Chicago.

Schott, J., Pokrovsky, O. S., & Oelkers, E. H. (2009). The Link Between Mineral Dissolution/Precipitation Kinetics and Solution Chemistry. *Reviews in Mineralogy and Geochemistry*, *70*(1), 207 - 258. Retrieved from http://rimg.geoscienceworld.org/content/70/1/207.abstract doi: 10.2138/rmg.2009.70.6

Siebert, C., Nägler, T., & Kramers, J. (2001). Determination of molybdenum isotope fractionation by double-spike multicollector inductively coupled plasma mass spectrometry. *Geochemistry Geophysics Geosystems*, *2*. Retrieved from http://www.agu.org/journals/gc/gc0107/2000GC000124/a2000GC000124.html

Sollins, P., Sancho M., F., Mata Ch., R., & Sanford Jr., R. L. (1994). Soils and soil process research. In *La selva: Ecology and natural history of a tropical rainforest* (pp. 34–53). University of Chicago Press.

Sparks, J. P., Chandra, S., Derry, L. a., Parthasarathy, M. V., Daugherty, C. S., & Griffin, R. (2010, 7). Subcellular localization of silicon and germanium in grass root and leaf tissues by SIMS: evidence for differential and active transport. *Biogeochemistry*, *104*(1-3), 237–249. Retrieved from http://link.springer.com/10.1007/s10533-010-9498-2 doi: 10.1007/s10533-010-9498-2

Street-Perrott, F. A., & Barker, P. A. (2008). Biogenic silica: a neglected component of the coupled global continental biogeochemical cycles of carbon and silicon. *Earth Surface Processes and Landforms*, *33*(9), 1436–1457. Retrieved from http://dx.doi.org/10.1002/esp.1712 doi: 10.1002/esp.1712

Struyf, E., Smis, A., Damme, S., Meire, P., & Conley, D. J. (2010, 2). The Global Biogeochemical Silicon Cycle. *Silicon*, *1*(4), 207–213. Retrieved from http://www.springerlink.com/index/10.1007/s12633-010-9035-x doi: 10.1007/s12633-010-9035-x

Tricca, A., Porcelli, D., & Wasserburg, G. J. (2000). Factors controlling the groundwater transport of U, Th, Ra, and Rn. *Proceedings of the Indian Academy of Sciences, Earth and Planetary Sciences*, *109*(1), 95–108. doi: 10.1007/BF02719153

Veldkamp, E., Becker, A., Schwendenmann, L., Clark, D. J. a., & Schulte-Bisping, H. (2003). Substantial labile carbon stocks and microbial activity in deeply weathered soils below a tropical wet forest. *Global Change Biology*, *9*, 1171–1184. doi: 10.1046/j.1365-2486.2003.00656.x

Walker, J. C., Hays, P., & Kasting, J. (1981). A negative feedback mechanism for the long-term stabilization of Earth's surface temperature. *Journal of Geophysical Research*, *86*(C10), 9776–9782. Retrieved from http://dx.doi.org/10.1029/JC086iC10p09776 doi: 10.1029/JC086iC10p09776

Watkins, J. M., DePaolo, D. J., & Watson, E. B. (2017, 1). Kinetic Fractionation of Non-Traditional Stable Isotopes by Diffusion and Crystal Growth Reactions. *Reviews in Mineralogy and Geochemistry*, *82*(1), 85–125. Retrieved from http://rimg.geoscienceworld.org/lookup/doi/10.2138/rmg.2017.82.4 doi: 10.2138/rmg.2017.82.4

White, A. F., Vivit, D. V., Schulz, M. S., Bullen, T. D., Evett, R. R., & Aagarwal, J. (2012, 10). Biogenic and pedogenic controls on Si distributions and cycling in grasslands of the Santa Cruz soil chronosequence, California. *Geochimica et Cosmochimica Acta*, *94*, 72–94. Retrieved from http://linkinghub.elsevier.com/retrieve/pii/S0016703712003614 doi: 10.1016/j.gca.2012.06.009

Zachos, J., Pagani, M., Sloan, L., Thomas, E., & Billups, K. (2001, 4). Trends, rhythms, and aberrations in global climate 65 Ma to present. *Science*, *292*(5517), 686–93. Retrieved from http://www.ncbi.nlm.nih.gov/pubmed/11326091 doi: 10.1126/science.1059412

Ziegler, K., Chadwick, O. A., Brzezinski, M. A., & Kelly, E. F. (2005, 10). Natural variations of d30Si ratios during progressive basalt weathering, Hawaiian Islands. *Geochimica et Cosmochimica Acta*, *69*(19), 4597–4610. Retrieved from http://linkinghub.elsevier.com/retrieve/pii/S001670370500431X doi: 10.1016/j.gca.2005.05.008

Acknowledgments

All data discussed in this study are given in the main and supplementary tables. During revision, all data are attached in tabulated form as a MS Excel file. Upon acceptance, data will be added to an appropriate repository.

This work was financially supported by the UK Natural Environment Research Council (NERC grant NE/H012656/1 to AJW and KWB) and US National Science Foundation (NSF grant OCE-1260692 to DEH). JJB was additionally supported by the John Montagne Award (Quaternary Geology & Geomorphology division, GSA), and the InterRidge Research Fellowship. Support for SO was provided by the Fonds National de la Recherche Scientifique (FNRS), Belgium. OR was supported by the Institut Carnot Ifremer EDROME and the LabexMer ANR-10-LABX-19-01. Field work was hosted by the Institute of Tropical Studies, La Selva Research Station. We thank Emmanuel Ponzavera for assisting with Ge isotope analyses at Ifremer.

Supplementary Material: Ge and Si isotope behavior during intense tropical weathering

J. Jotautas Baronas[1,2], A. Joshua West[1], Kevin W. Burton[3],Douglas E. Hammond[1],

Sophie Opfergelt[4], Philip A.E. Pogge von Strandmann[5], Rachael H. James[6],

Olivier Rouxel[7]

[1]Department of Earth Sciences, University of Southern California, Los Angeles, CA 90089, USA

[2]Department of Earth Sciences, University of Cambridge, Cambridge CB2 3EQ, UK

[3]Department of Earth Sciences, Durham University, Durham DH1 3LE, UK

[4]Earth and Life Institute, Université catholique de Louvain, Croix du Sud bte L7.05.10, 1348 Louvain-la-Neuve, Belgium

[5]London Geochemistry and Isotope Centre (LOGIC), Institute of Earth and Planetary Sciences, University College London and Birkbeck, University of London, Gower Street, London WC1E 6BT, UK

[6]School of Ocean and Earth Science, National Oceanography Centre Southampton, University of Southampton Waterfront Campus, Southampton SO14 3ZH, UK

[7]IFREMER, Centre de Brest, Unité Géosciences Marines, 29280 Plouzané, France

Contents of this file

Introduction

Dataset S1 contains all data presented in this study, tabulated as a MS Excel file. Tables S1-S2 and Figures S1,S2, and S6 show additional data on measured samples, as discussed in text. Text S1 describes in detail the reactive transport model used to simulate the chemical evolution of interbasin groundwater (IBGW) during transit (associated Table S3, Fig. S3-S4). Text S1 describes in detail the isotope mass balance model used to constrain the contemporary Ge and Si cycle in lowland soils (associated Tables S4-S5, Fig. S5).

Text S1. Interbasin groundwater reactive transport model

Model description

The concentration and isotopic composition of solutes like Si and Ge in flowing groundwater are affected by 1) advection; 2) dissolution of primary silicate minerals; and 3) precipitation of secondary phases incorporating the element of interest. The exact mechanism of Si and Ge removal from solution is not specified in the model. It could therefore be conceived as either net adsorption, co-precipitation, or a combination of both processes, as long as it follows first order reaction kinetics (see below). For simplicity, in the following text we usually refer to Ge and Si removal from solution as "precipitation". Diffusion effects are assumed to be negligible relative to the rate of fluid advection. Assuming that the shape of the fluid composition profile along the flowpath does not change with time, the change in dissolved groundwater Si concentration along the flowpath can be determined as:

$$\frac{d[^{28}Si]_{fluid}}{dx} = \left(\frac{\rho_{rock} \cdot (1-\phi)}{\rho_{fluid} \cdot \phi}\right) \cdot [^{28}Si]_{rock} \cdot \frac{^{28}k_{diss}}{q} - [^{28}Si]_{fluid} \cdot \frac{^{28}k_{sec}}{q} \quad (1)$$

where $[^{28}Si]$ is the concentration of ^{28}Si isotope in [μmol L^{-1}], x is distance in [m], ρ is density in [gcm^{-3}], q is fluid flow rate in [ms^{-1}] and $^{28}k_{diss}$ and $^{28}k_{sec}$ are the first-order rate constants of dissolution and precipitation, respectively, in [s^{-1}] (all parameter definitions and used values are summarized in Table S3). The first term represents the release of Si from the dissolution of primary minerals and the second term represents removal (precipitation or adsorption) of Si with secondary phases. The Si-specific dissolution rate [$mol\ Si\ m^{-2}\ s^{-1}$] is obtained from:

$$r_{diss}^{Si} = r_{diss}^{min} \cdot f_{min} \cdot X_{min}^{Si} \tag{2}$$

and then the first-order rate constant [s^{-1}] from:

$$^{28}k_{diss} = r_{diss}^{Si} \cdot A_{rock} \cdot M_{min} \tag{3}$$

where r_{diss}^{min} is the far-from-equilbrium primary mineral dissolution rate in [$mol\ m^{-2}\ s^{-1}$], A_{rock} is the specific bulk rock surface area in [$m^2\ g^{-1}$], M_{min} is the molar mass of the dissolving mineral in [$g\ mol^{-1}$], f_{min} is the weight fraction of the dissolving mineral in the bulk rock, and X_{min}^{Si} is the stoichiometry of Si in the mineral [$mol\ Si\ /mol\ mineral$]).

Integrating Eq. 1 for boundary conditions $[^{28}Si]_{fluid} = [^{28}Si]_{fluid}^{0}$ when x = 0 and $[^{28}Si]_{fluid} = [^{28}Si]_{fluid}^{x}$ when x = x yields:

$$[^{28}Si]_{fluid}^{x} = \left(\frac{\rho_{rock} \cdot (1-\phi)}{\rho_{fluid} \cdot \phi}\right) \cdot [^{28}Si]_{rock} \cdot \frac{^{28}k_{diss}}{^{28}k_{sec}} \cdot \left(1 - e^{\left(-^{28}k_{sec} \cdot \frac{x}{q}\right)}\right) + [^{28}Si]_{fluid}^{0} \cdot e^{\left(-^{28}k_{sec} \cdot \frac{x}{q}\right)} \tag{4}$$

Equation 4 describes the concentration of an isotope at a given point along the fluid flowpath, as a function of the rates of addition (via primary mineral dissolution) and removal (via secondary phase adsorption or secondary phase precipitation). At a certain point along the flowpath, as

$x \gg \frac{q}{^{28}k_{sec}}$, the age of fluid $t_{fluid} = \frac{x}{q}$ exceeds the residence time of Si in solution $\tau_{res} = \frac{1}{^{28}k_{sec}}$, the exponential terms in Eq. 4 approach zero, and $[^{28}Si]^{x}_{fluid}$ approaches steady state:

$$[^{28}Si]^{ss}_{fluid} = \left(\frac{\rho_{rock} \cdot (1-\phi)}{\rho_{fluid} \cdot \phi}\right) \cdot [^{28}Si]_{rock} \cdot \frac{^{28}k_{diss}}{^{28}k_{sec}} \tag{5}$$

Using the values for the various parameters given in Table S3, Eqs. 3 and 5 can be used to calculate $^{28}k_{sec}$ (Table S3). It must be noted here that these first-order rate constants are assumed to be constant, implying that the assemblage of dissolving and precipitating minerals remains unchanged along the groundwater flowpath.

An equivalent set of equations can be written for $[^{30}Si]$. The isotopic fractionation factors associated with dissolution and precipitation are defined as $^{30/28}\alpha_{diss} = {}^{30}k_{diss}/{}^{28}k_{diss}$ and $^{30/28}\alpha_{sec} = {}^{30}k_{sec}/{}^{28}k_{sec}$. Dividing Eq. 4 for ^{30}Si by that for ^{28}Si, plugging in the α expressions given above, and performing some algebraic manipulation yields an expression for the isotopic ratio of dissolved Si:

$$\left(\frac{^{30}Si}{^{28}Si}\right)^{x}_{fluid} = \frac{[^{28}Si]^{ss}_{fluid}}{[^{28}Si]^{x}_{fluid}} \cdot \left(\frac{^{30}Si}{^{28}Si}\right)_{rock} \cdot \frac{^{30/28}\alpha_{diss}}{^{30/28}\alpha_{sec}} \cdot \left(1 - e^{\left(-^{28}k_{sec} \cdot ^{30/28}\alpha_{sec} \cdot \frac{x}{q}\right)}\right) + \tag{6}$$

$$+ \frac{[^{28}Si]^{0}_{fluid}}{[^{28}Si]^{x}_{fluid}} \cdot \left(\frac{^{30}Si}{^{28}Si}\right)^{0}_{x} \cdot e^{\left(-^{28}k_{sec} \cdot ^{30/28}\alpha_{sec} \cdot \frac{x}{q}\right)} \tag{7}$$

From Eq. 6, as $x \gg \frac{q}{^{28}k_{sec}}$, the dissolved Si isotope ratio approaches steady state:

$$\left(\frac{^{30}Si}{^{28}Si}\right)^{ss}_{fluid} = \frac{^{30/28}\alpha_{diss}}{^{30/28}\alpha_{sec}} \cdot \left(\frac{^{30}Si}{^{28}Si}\right)_{rock} \tag{8}$$

The net fractionation factor is then:

$$^{30/28}\alpha_{net} = \frac{^{30/28}\alpha_{diss}}{^{30/28}\alpha_{sec}} \quad (9)$$

Assuming congruent mineral dissolution $^{30}k_{diss} = {}^{28}k_{diss}$ and therefore $^{30/28}\alpha_{diss} = 1$. Most field and experimental data suggest little to no fractionation during silicate mineral dissolution (Frings et al., 2016).

Similar equations can be written for germanium isotopes ^{74}Ge and ^{70}Ge to calculate the [Ge] and $\delta^{74}Ge$ evolution of the IBGW fluid, which also yields an expression of the fluid Ge/Si ratio along the pathway. Since the total dissolution and the net release (i.e., addition to solution) rates are known for each element, they can be combined to calculate the $\delta^{30}Si$, $\delta^{74}Ge$, and Ge/Si composition of the precipitating secondary phases at any given point.

Model application

For simplicity, the primary dissolving mineral is taken to be albite; therefore a typical plagioclase Ge/Si ratio of 3 μmol/mol is used instead of the 2.1-2.3 μmol/mol measured in the bulk rock (Table 1). The bulk rock has a lower ratio due to the presence of quartz, which typically has Ge/Si of $\sim 0.5\mu$mol/mol (Murnane & Stallard, 1990; Kurtz et al., 2002) and is assumed to not dissolve to any appreciable extent in the presence of other more labile silicate minerals. For $\delta^{74}Ge$ and $\delta^{30}Si$, we assume that plagioclase is identical to the bulk rock, which is reasonable given the relatively small variations in Ge and Si isotopic signatures of various silicate rocks (Escoube et al., 2012; Frings et al., 2016). Finally, we assume no $\delta^{74}Ge$ fractionation during plagioclase dissolution, i.e. $^{74/70}\alpha_{diss} = 1$.

To account for the kinetic rate dependence on the distance to equilibrium, we use a simple expression of the transition state theory (TST) (Schott et al., 2009). The albite ion activity product

and saturation (Ω) values for the initial fluid (represented by rainwater sample LS16) and the final steady state fluid (represented by the IBGW sample CR05) are calculated using data in Table 2 and Geochemist's Workbench Edition 11.0. As expected, rainwater is highly undersaturated ($SI = log(\Omega) = -5.9$), whereas the final IBGW fluid is supersaturated ($SI = 0.6$) with respect to albite. Since Al, Na, and other solutes are not modeled along the flowpath, albite saturation is assumed to be a linear function of the evolving dissolved Si concentration. Then, albite dissolution rate approaches zero as Ω approaches 1. We also assume that albite precipitation rates are negligible under these conditions even when Ω is slightly above 1. The use of a different primary silicate mineral would influence the selection of a dissolution rate constant and initial Ge/Si ratio, but would not otherwise have a major impact on the model results.

The solution volume-normalized Si dissolution rate in $[mol\ L^{-1}\ s^{-1}]$ is calculated as:

$$'r_{diss}^{Si} = r_{diss}^{Si} \cdot A_{rock} \cdot \frac{\rho_{rock}}{\phi} \cdot (1 - \Omega) \tag{10}$$

where r_{diss}^{Si} is the mineral-normalized dissolution rate in $[mol\ m^{-2}\ s^{-1}]$ (Eq. 2). The secondary Si removal rate can then be calculated as the difference between $'r_{diss}^{Si}$ and the net Si addition to solution over a given section of the fluid flowpath calculated using Eq. 4. The evolution of the Si dissolution and precipitation rates as a function of distance and $[Si]_{fluid}$ is shown in Fig. S3. The dissolution and precipitation rates for Ge can be obtained in the same way. The absolute values depend primarily on the intrinsic mineral dissolution rate supplied to the model (Table S3). To provide a conservative estimate for the fluid equilibration lengthscale (or timescale), this value was chosen from the lower end of plagioclase weathering rates derived using field data (Brantley et al., 2008). The other parameters supplied to the model, such as rock surface area,

fraction of reactive mineral, and porosity (Table S3) have a minor effect on the model output relative to the dissolution rate.

It must be noted that the dissolved Si concentration in the IBGW fluid is ~3 times higher than the highest values observed in most low-temperature weathering fluids (~400 μmol/L) that are assumed to represent the thermodynamic limit for systems where primary minerals are dissolving and secondary phases are precipitating (Maher & Chamberlain, 2014). This could be the result of elevated temperatures within the slopes of Barva Volcano, or more likely, enhanced solubility of primary silicates and secondary minerals due to high acidity resulting from the degassing and dissolution of magmatic CO_2 into the groundwater (Genereux et al., 2009). Although both temperature and pH measured in IBGW (Table 2) were no different from other local streams, the high alkalinity, as well as previous studies of $\delta^{13}C$ and other tracers in this fluid (Genereux et al., 2009) suggest significant input of magmatic CO_2 that had been neutralized via reaction with the volcanic silicate rock during transit. If IBGW is indeed initially acidic and CO_2-enriched, it would imply higher silicate dissolution rates than those used in the present modeling scenario and shorter equilibration lengthscale. The equilibration lengthscale calculated here should thus be considered a conservative maximum estimate.

The modeled evolution of the IBGW fluid composition is shown in Fig. S4. Note that while a true chemical equilibrium is achieved within about 3000 m (Fig. S3), steady state dissolved Ge and Si concentrations are achieved within about 200 and 1500 m, respectively, and steady state $\delta^{74}Ge$ and $\delta^{30}Si$ compositions within about 400 and 2500 m, respectively. All distances were calculated assuming a flow rate of 3 m/y, based on dissolved organic radiocarbon dating (Genereux et al., 2009). Therefore, the assumption that IBGW fluid represents a fully

equilibrated steady state composition appears to be robust, especially given the low value of the mineral dissolution rate used in these calculations (Table S3).

Text S2. Lowlands isotopic mass balance model

We use the mixed open system model previously described in detail by Baronas et al. (2018), with some slight implementation changes which are described below. Briefly, the model applies a simple mass balance equation to proxy signatures (in this case, Ge/Si, $^{30}Si/^{28}Si$, and $^{74}Ge/^{70}Ge$) to determine the partitioning of a given element (in this case, Si and Ge) between different phases:

$$R_{ini} = \sum R_i \cdot f_i^X = R_{sec} \cdot f_{sec}^X + R_{bio} \cdot f_{bio}^X + R_{diss} \cdot f_{diss}^X \tag{11}$$

$$f_{sec}^X + f_{bio}^X + f_{diss}^X = 1 \tag{12}$$

where f^X is the molar fraction of species X in the denominator of ratio R, where *ini* is the initial dissolving material (e.g. bedrock, or in this case, the average composition of bulk soil), *sec* represents the sum of neoforming secondary mineral phases (represented by the composition of separated clays), *bio* is the sum of biological phases (in this case represented by vegetation samples), and *diss* is the remaining dissolved phase (represented by soil pore waters, or alternatively stream and groundwater samples in the Taconazo watershed; see below). All values used as model inputs are summarized in Table S4 and the model outputs in Table S5.

Fractionation factors are defined as:

$$\alpha_{sec}^R = \frac{R_{sec}}{R_{diss}} \tag{13}$$

$$\alpha_{bio}^{R} = \frac{R_{bio}}{R_{diss}} \tag{14}$$

where R is the elemental or isotopic ratio of interest. Equations 11-14 can be combined, rearranged, and applied to Si isotope ratios (R = $^{30}Si/^{28}Si$) to obtain:

$$f_{sec}^{Si} = \frac{\frac{R_{ini}}{R_{diss}} - f_{diss}^{Si} \cdot (1 - \alpha_{bio-diss}^{30/28}) - \alpha_{bio-diss}^{30/28}}{\alpha_{sec-diss}^{30/28} - \alpha_{bio-diss}^{30/28}} \tag{15}$$

where $f^{Si} \approx f^{^{28}Si}$. In the case of La Selva soils, all the parameters on the right-hand side of Eq. 15 are known from measurements (Table S4), with the exception of f_{diss}^{Si}, which is determined from:

$$f_{diss}^{Si} = \frac{(Si/Na)_{diss}}{(Si/Na)_{ini}} \tag{16}$$

The fraction of Si taken up by vegetation is then simply:

$$f_{bio}^{Si} = 1 - f_{sec}^{Si} - f_{diss}^{Si} \tag{17}$$

The partitioning of Ge mass balance is determined the same way, with Ge uptake by secondary phases

$$f_{sec}^{Ge} = f_{sec}^{Si} \cdot \frac{(Ge/Si)_{sec}}{(Ge/Si)_{ini}} \tag{18}$$

and vegetation

$$f_{bio}^{Ge} = 1 - f_{sec}^{Ge} - f_{diss}^{Ge} \tag{19}$$

yielding a prediction of vegetation Ge/Si ratio

$$(Ge/Si)_{bio} = (Ge/Si)_{ini} \cdot \frac{f_{bio}^{Ge}}{f_{bio}^{Si}} \tag{20}$$

and thus biological fractionation factor, which can be defined either relative to the dissolved phase

$$\alpha_{bio}^{Ge/Si} = \frac{(Ge/Si)_{bio}}{(Ge/Si)_{diss}} \tag{21}$$

or the initial substrate (i.e., bulk soil in this case)

$$K_{bio} = \frac{(Ge/Si)_{bio}}{(Ge/Si)_{ini}} \tag{22}$$

Equivalent Ge/Si fractionation factors are calculated for uptake via secondary mineral phases. The secondary phase fractionation factor $\alpha_{sec}^{74/70}$ (i.e., $\Delta^{74}Ge_{sec-diss}$ when expressed in parts-per-thousand) is determined using Eq. 13 and the measured composition of clays and bulk soils (Table S4). Equation 11 can then be applied to calculate $\delta^{74}Ge_{bio}$. However, due to the very low mass fraction of Ge taken up by vegetation in this case ($f_{bio}^{Ge} < 0.1$; Table S5), the estimate of $\delta^{74}Ge_{bio}$ and consequently $\Delta^{74}Ge_{bio}$ is extremely uncertain and not reported here.

The calculations described above were implemented as MATLAB code and repeated 10 million times, randomly sampling from the uncertainty range of the input parameters (Table S4). Model runs resulting in certain physically impossible values (e.g., any f values <0 or >1) have been removed. An additional restriction was applied that $\alpha_{bio}^{Ge/Si} < 1$, i.e. vegetation uptake fractionating against Ge relative to Si, in agreement with the vast majority of studies that have reported $\alpha_{bio}^{Ge/Si}$ values for a wide range of plants (see references in main text). After filtering, about 500,000 model runs were retained. We report the median, standard deviation, and interquartile ranges of all parameters from these retained model runs (Table S5). Probability

distribution of Ge and Si partitioning between secondary mineral and vegetation phases is additionally shown in Fig. S5.

References

Baronas, J. J., Torres, M. A., West, A. J., Rouxel, O. J., Georg, R. B., Bouchez, J., ... Hammond, D. E. (2018, 12). Ge and Si isotope signatures in rivers: A quantitative multi-proxy approach. *Earth and Planetary Science Letters*, *503*, 194–215. Retrieved from https://linkinghub.elsevier.com/retrieve/pii/S0012821X18305612 doi: 10.1016/j.epsl.2018.09.022

Brantley, S., Kubicki, J., & White, A. (2008). *Kinetics of water-rock interaction* (S. Brantley, J. Kubicki, & A. White, Eds.). New York: Springer. Retrieved from http://link.springer.com/content/pdf/10.1007/978-0-387-73563-4.pdf

Escoube, R., Rouxel, O. J., Luais, B., Ponzevera, E., & Donard, O. F. (2012, 6). An Intercomparison Study of the Germanium Isotope Composition of Geological Reference Materials. *Geostandards and Geoanalytical Research*, *36*(2), 149–159. Retrieved from http://doi.wiley.com/10.1111/j.1751-908X.2011.00135.x doi: 10.1111/j.1751-908X.2011.00135.x

Frings, P. J., Clymans, W., Fontorbe, G., De La Rocha, C. L., & Conley, D. J. (2016, 5). The continental Si cycle and its impact on the ocean Si isotope budget. *Chemical Geology*, *425*, 12–36. Retrieved from http://dx.doi.org/10.1016/j.chemgeo.2016.01.020http://linkinghub.elsevier.com/retrieve/pii/S0009254116300201 doi: 10.1016/j.chemgeo.2016.01.020

Froelich, P., Blanc, V., Mortlock, R., Chillrud, S., Dunstan, W., Udomkit, A., & Peng, T.

(1992). River fluxes of dissolved silica to the ocean were higher during glacials: Ge/Si in diatoms, rivers, and oceans. *Paleoceanography*, *7*(6), 739–767. Retrieved from http://www.agu.org/pubs/crossref/1992.../92PA02090.shtml

Genereux, D. P., Jordan, M. T., & Carbonell, D. (2005). A paired-watershed budget study to quantify interbasin groundwater flow in a lowland rain forest, Costa Rica. *Water Resources Research*, *41*, 1–17. doi: 10.1029/2004WR003635

Genereux, D. P., Webb, M., & Solomon, D. K. (2009, 8). Chemical and isotopic signature of old groundwater and magmatic solutes in a Costa Rican rain forest: Evidence from carbon, helium, and chlorine. *Water Resources Research*, *45*(8). Retrieved from http://doi.wiley.com/10.1029/2008WR007630 doi: 10.1029/2008WR007630

Kurtz, A., Derry, L., & Chadwick, O. (2002). Germanium-silicon fractionation in the weathering environment. *Geochimica et Cosmochimica Acta*, *66*(9), 1525–1537. Retrieved from http://www.sciencedirect.com/science/article/pii/S0016703701008699

Maher, K., & Chamberlain, C. P. (2014, 3). Hydrologic regulation of chemical weathering and the geologic carbon cycle. *Science*, *343*(6178), 1502–4. Retrieved from http://science.sciencemag.org/content/343/6178/1502.long doi: 10.1126/science.1250770

Murnane, R., & Stallard, R. (1990). Germanium and silicon in rivers of the Orinoco drainage basin. *Nature*, *344*, 749–752. Retrieved from http://www.nature.com/nature/journal/v344/n6268/abs/344749a0.html

Schott, J., Pokrovsky, O. S., & Oelkers, E. H. (2009). The Link Between Mineral Dissolution/Precipitation Kinetics and Solution Chemistry. *Reviews in Mineralogy and Geochemistry*, *70*(1), 207 - 258. Retrieved from http://rimg.geoscienceworld.org/content/70/1/207.abstract doi: 10.2138/rmg.2009.70.6

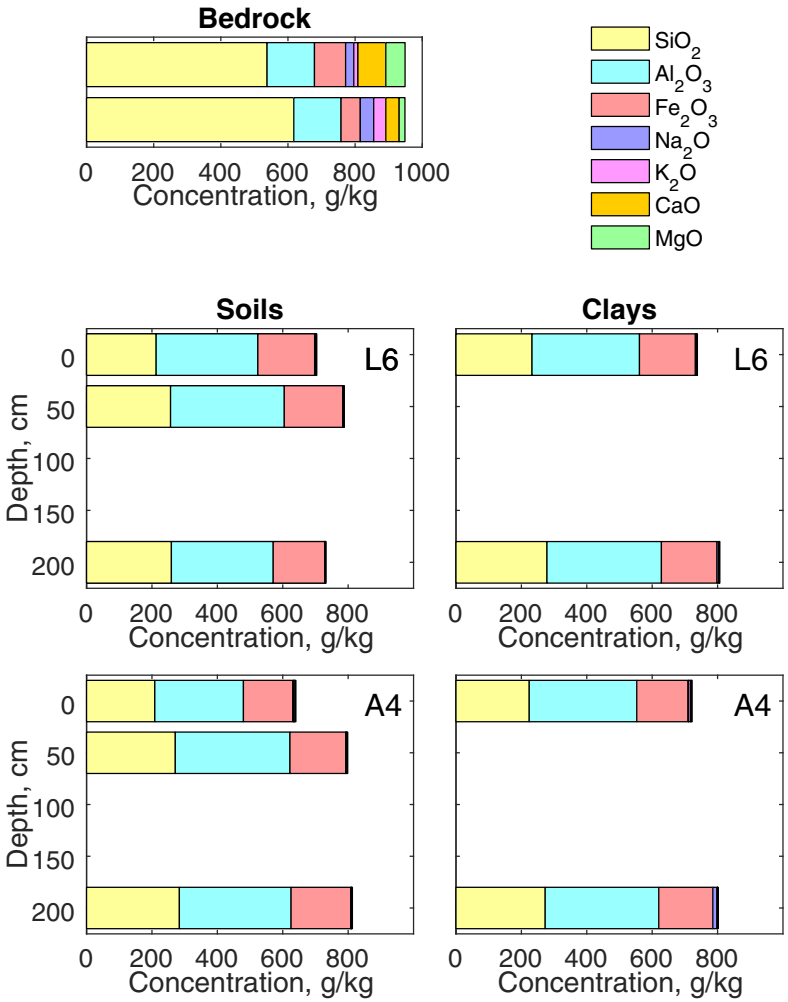

Figure S1. Elemental composition of bedrock, bulk soils, and separated clays in La Selva.

Table S1. Chemical alteration of soils and river sediments relative to parent bedrock, calculated relative to Ti using Eq. 4.

Sample	Depth	T_{Al}	T_{Fe}	T_{Si}	T_{Na}	T_{K}	T_{Ca}	T_{Mg}	T_{Mn}	T_{Ge}
Bulk soils										
Soil pit A4	0 cm	0.02	0.08	-0.81	-0.99	-0.94	-0.98	-0.95	-0.58	-0.46
Soil pit A4	50 cm	0.22	0.12	-0.77	-0.99	-0.95	-1.00	-0.96	-0.37	--
Soil pit A4	200 cm	0.09	0.10	-0.78	-1.00	-0.98	-1.00	-0.97	-0.76	-0.34
Soil pit L6	0 cm	0.19	0.25	-0.80	-0.99	-0.96	-1.00	-0.95	-0.86	-0.43
Soil pit L6	50 cm	0.30	0.25	-0.77	-0.99	-0.97	-1.00	-0.96	-0.84	-0.33
Soil pit L6	200 cm	0.31	0.24	-0.73	-1.00	-0.97	-1.00	-0.97	-0.87	-0.20
Bedload										
LS01 (bulk)	--	0.15	-0.07	-0.64	-0.85	-0.81	-0.80	-0.84	-0.41	--
LS02 (bulk)	--	0.24	0.00	-0.52	-0.70	-0.66	-0.63	-0.71	-0.58	--
Suspended load										
LS01 (Taconazo)	0 m	0.31	0.10	-0.66	-0.94	-0.89	-0.94	-0.94	-0.68	--
LS02 (Arboleda at weir)	0 m	0.31	0.37	-0.61	-0.78	-0.72	-0.76	-0.82	-0.62	--
LS04 (El Salto)	0 m	0.35	0.56	-0.96	-0.93	-0.95	-0.94	-0.96	-0.14	--
LS15 (Arboleda upstream)	0 m	0.20	0.03	-0.89	-0.99	-0.96	-0.99	-0.98	-0.80	--

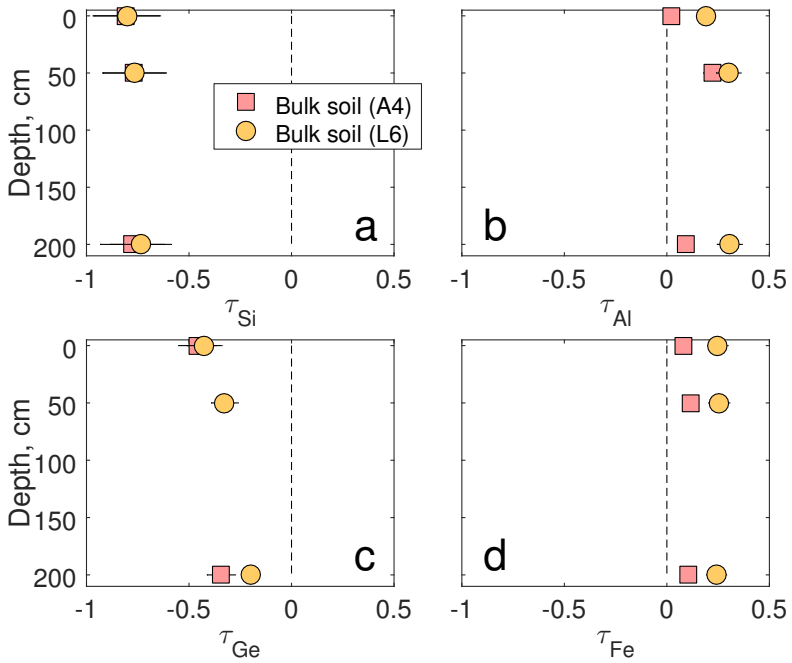

Figure S2. Chemical alteration of bulk soils relative to parent bedrock, calculated relative to Ti using Eq. 4.

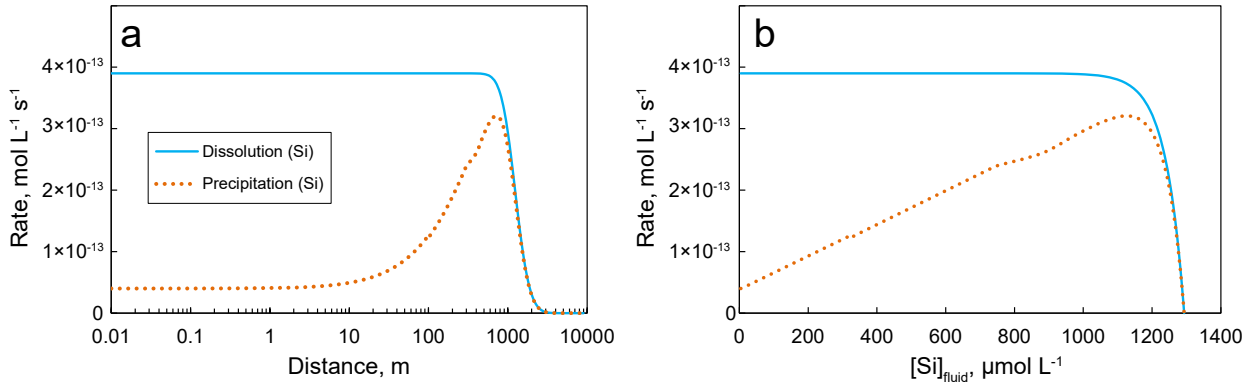

Figure S3. The modeled evolution of Si dissolution and precipitation rates ($'r^{Si}_{diss}$ and $'r^{Si}_{ppt}$, respectively) along the interbasin groundwater flowpath.

Table S2. Comparison of all measured $\delta^{30}Si$ and $\delta^{29}Si$ values. All samples show mass-dependent relationship.

Sample ID	δ^{30}Si ± 2σ (‰)	δ^{29}Si ± 2σ (‰)
LS01	0.29 ± 0.13	0.14 ± 0.09
LS02	1.03 ± 0.12	0.54 ± 0.10
LS04	0.46 ± 0.18	0.24 ± 0.11
LS05	1.27 ± 0.21	0.87 ± 0.13
LS06	1.12 ± 0.14	0.61 ± 0.11
LS07	1.03 ± 0.10	0.57 ± 0.08
LS08	0.57 ± 0.15	0.28 ± 0.10
LS09	0.70 ± 0.14	0.38 ± 0.14
LS10	0.92 ± 0.26	0.48 ± 0.11
LS11	0.67 ± 0.27	0.36 ± 0.13
LS12	0.64 ± 0.20	0.38 ± 0.10
LS13	1.23 ± 0.15	0.72 ± 0.12
LS14	0.38 ± 0.15	0.41 ± 0.13
LS15	0.19 ± 0.09	0.13 ± 0.24
LS17	1.03 ± 0.13	0.58 ± 0.08
CR01	1.32 ± 0.14	0.74 ± 0.16
CR02	1.34 ± 0.26	0.93 ± 0.17
CR03	1.52 ± 0.21	1.09 ± 0.11
CR04	-0.03 ± 0.24	0.20 ± 0.14
CR05	1.02 ± 0.24	0.77 ± 0.17
LS03	0.06 ± 0.13	0.06 ± 0.07
LS18	0.17 ± 0.14	0.14 ± 0.06
LS19	0.21 ± 0.18	0.22 ± 0.09
LS20	-0.67 ± 0.07	-0.20 ± 0.12
LS21	-0.40 ± 0.26	-0.06 ± 0.12
A4-0-W	-1.25 ± 0.08	-0.58 ± 0.03
A4-25-W	-1.02 ± 0.10	-0.51 ± 0.07
A4-50-W	-1.21 ± 0.08	-0.59 ± 0.05
A4-200-W	-0.96 ± 0.09	-0.48 ± 0.07
L6-0-W	-0.03 ± 0.11	0.01 ± 0.02
L6-50-W	-1.04 ± 0.08	-0.52 ± 0.10
L6-200-W	0.02 ± 0.10	0.01 ± 0.08
LS-R1	-0.13 ± 0.18	-0.01 ± 0.02
LS-R2	-0.09 ± 0.25	-0.08 ± 0.02
A4-0-B	-1.74 ± 0.21	-0.84 ± 0.10
A4-50-B	-2.11 ± 0.23	-1.10 ± 0.10
A4-200-B	-1.88 ± 0.16	-0.95 ± 0.05
L6-0-B	-2.05 ± 0.19	-1.02 ± 0.10
L6-50-B	-2.19 ± 0.18	-1.19 ± 0.04
L6-200-B	-2.47 ± 0.25	-1.25 ± 0.07
A4-0-C	-2.60 ± 0.23	-1.28 ± 0.04
A4-200-C	-2.44 ± 0.07	-1.21 ± 0.04
L6-0-C	-2.69 ± 0.15	-1.34 ± 0.06
L6-200-C	-2.37 ± 0.09	-1.14 ± 0.04
A4-V	-1.90 ± 0.11	-0.92 ± 0.04
L6-V	-1.78 ± 0.19	-0.93 ± 0.05
LS01-B	-1.44 ± 0.09	-0.64 ± 0.07
LS01-C	-2.52 ± 0.13	-1.27 ± 0.04
LS02-B	-1.06 ± 0.07	-0.51 ± 0.03
LS01-S	-1.91 ± 0.17	-0.90 ± 0.10
LS02-S	-1.34 ± 0.17	-0.62 ± 0.10
LS04-S	-2.37 ± 0.12	-1.18 ± 0.04
LS15-S	-2.59 ± 0.14	-1.28 ± 0.05

Table S3. The description of parameters and values used in the reactive transport model of interbasin groundwater (IBGW) composition.

Parameter	Description	Value	Units	Source
φ	Porosity	0.1	-	Genereux et al. (2009)
ρ_{rock}	Rock density	2.6	g cm^{-3}	
ρ_{water}	Water density	1.0	g cm^{-3}	
q	IBGW flow rate	3	m y^{-1}	Genereux et al. (2009)
A_{rock}	Rock-specific surface area	0.1	m^2 g^{-1}	
M_{min}	Mineral molar mass	263	g mol^{-1}	Albite
f_{min}	Fraction of dissolving mineral in rock	0.5	-	
r^{min}_{diss}	Mineral dissolution rate constant	10^{-16}	mol m^{-2} s^{-1}	Brantley et al. (2008)
X^{Si}_{min}	Stoichiometric Si / mineral ratio	3	mol mol^{-1}	Albite
$[^{28}Si]_{rock}$	^{28}Si concentration in rock ($\approx[Si]_{rock}$)	0.0114	mol g^{-1}	Samples LS-R1,-R2 (Table 1)
$[^{28}Si]^0_{fluid}$	Initial fluid Si concentration ($\approx[Si]_{rain}$)	3.8	µmol L^{-1}	Sample LS16 (Table 2)
$[^{28}Si]^{ss}_{fluid}$	IBGW fluid Si concentration ($\approx[Si]_{IBGW}$)	1293	µmol L^{-1}	Sample CR05 (Table 2)
$(Ge/Si)_{albite}$	Ge/Si ratio in dissolving mineral	3	µmol mol^{-1}	Froelich et al. (1992), Kurtz et al. (2002)
X^{Ge}_{min}	Stoichiometric Ge / mineral ratio	9	µmol mol^{-1}	(= X^{Si}_{min} * $(Ge/Si)_{albite}$)
$[Ge]_{rock}$	Ge concentration in rock	0.0342	µmol g^{-1}	(= $[Si]_{rock}$ * $(Ge/Si)_{albite}$)
$[Ge]^0_{fluid}$	Initial fluid Ge concentration (=$[Ge]_{rain}$)	8.8	pmol L^{-1}	Sample LS16 (Table 2)
$[Ge]^{ss}_{fluid}$	IBGW fluid Ge concentration (=$[Ge]_{IBGW}$)	405	pmol L^{-1}	Sample CR05 (Table 2)
k^{Si}_{sec}	Si precipitation rate constant far-from-eq.	2.9×10^{-10}	s^{-1}	Eq. B2; $\Omega << 1$
k^{Ge}_{sec}	Ge precipitation rate constant far-from-eq.	2.3×10^{-9}	s^{-1}	Eq. B2; $\Omega << 1$
$^{30/28}\alpha_{diss}$	^{30}Si/^{28}Si dissolution fractionation	1	-	see text
$^{74/70}\alpha_{diss}$	^{74}Ge/^{70}Ge dissolution fractionation	1	-	see text
$^{30/28}\alpha_{sec}$	^{30}Si/^{28}Si fractionation during sec. phase precipitation	0.9988	-	($=\Delta^{30}Si_{sec} = \delta^{30}Si_{rock} - \delta^{30}Si_{IBGW}$ = -1.2±0.3‰); see main text
$^{74/70}\alpha_{sec}$	^{74}Ge/^{70}Ge fractionation during sec. phase precipitation	0.9970	-	($=\Delta^{74}Ge_{sec} = \delta^{74}Ge_{rock} - \delta^{74}Ge_{IBGW}$ = -3.0±0.9‰); see main text

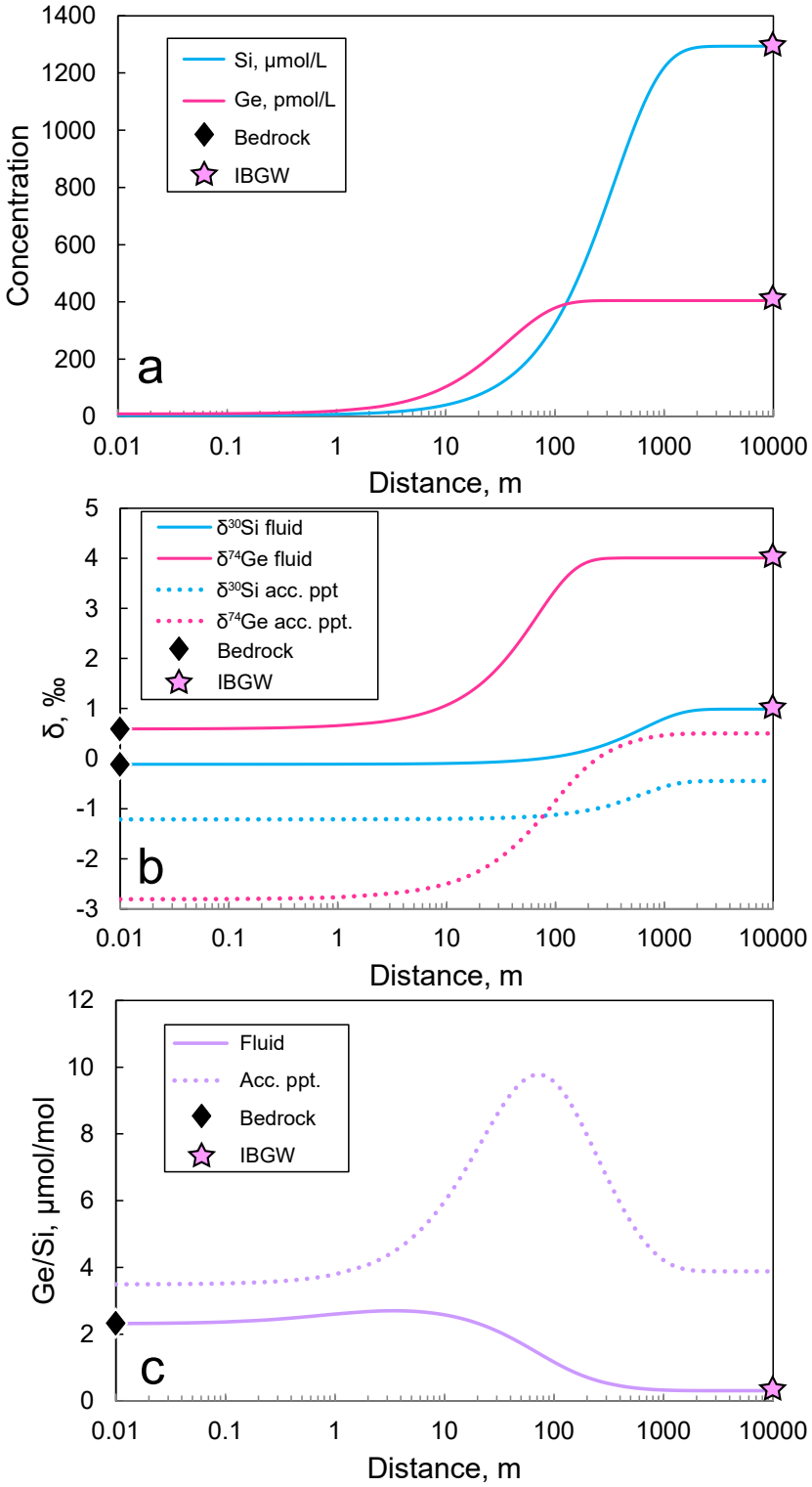

Figure S4. The modeled evolution of fluid chemistry along the interbasin groundwater (IBGW) flowpath. Panel (a) shows dissolved Si and Ge concentration, panel (b) shows the isotopic composition of the fluids and the accumulated secondary precipitates, and panel (c) shows the Ge/Si ratio in the fluid and the accumulated precipitates. The model assumes first order reaction kinetics and constant solid reactivity along the flow path length. Fluid velocity is set to 3 m/y (Genereux et al., 2005).

Table S4. Composition of the different phases used to partition the Ge and Si mass balance in La Selva soils. Values are simple means of collected sample types. Taconazo water refers to the mean of all stream and shallow groundwater samples in the Taconazo watershed (LS01, LS12, LS14, LS18). * Indicates that dissolved Na concentrations have been corrected for cyclic salt inputs (= $[Na]-0.86[Cl]$). # Ge/Si and $\delta^{74}Ge$ values of pore waters were not measured due to insufficient sample volume. The values used in the model were thus extrapolated from measured pore water $\delta^{30}Si$ values, using the close correlation between measured $\delta^{30}Si$, Ge/Si, and $\delta^{74}Ge$ across lowland fluid samples unaffected by IBGW (namely, LS01,-03,-12,-14,18-20, and CR01-03).

Phase (subscript)	Na (mol/kg)	Si (mol/kg)	Ge (µmol/kg)	Ge/Si (µmol/mol)	δ^{30}Si (‰)	δ^{74}Ge (‰)
Bulk soil (ini)	0.013 ± 0.004	4.2 ± 0.5	26.0 ± 3.6	6.32 ± 0.22	-2.07 ± 0.25	-0.13 ± 0.12
Clay (sec)	--	4.2 ± 0.5	30.8 ± 3.5	7.35 ± 0.47	-2.53 ± 0.15	-0.16 ± 0.09
Vegetation (bio)	--	--	--	--	-1.84 ± 0.09	--
	(µmol/L)	***(µmol/L)***	***(pmol/L)***			
Soil pore waters (diss)	33 ± 20 *	62 ± 33	138 ± 81	2.21 ± 0.46 #	-0.78 ± 0.50	2.13 ± 0.15 #
Taconazo water (diss)	13 ± 4 *	103 ± 34	101 ± 4	1.03 ± 0.27	0.37 ± 0.20	2.49 ± 0.13

Table S5. Isotopic mass balance model results for La Selva soils.

	Soil pore waters			*Taconazo water*
	Median	**1 st. dev.**	**25-75th perc.**	**25-75th perc.**
f^{Si}_{diss}	0.005	0.004	0.003 - 0.008	0.01 - 0.03
f^{Si}_{sec}	0.61	0.14	0.51 - 0.71	0.51 - 0.72
f^{Si}_{bio}	0.39	0.14	0.29 - 0.48	0.26 - 0.47
f^{Ge}_{diss}	0.002	0.002	0.001 - 0.004	0.003 - 0.006
f^{Ge}_{sec}	0.91	0.09	0.84 - 0.96	0.88 - 0.98
f^{Ge}_{bio}	0.09	0.09	0.04 - 0.16	0.02 - 0.11
$(Ge/Si)_{bio}$	1.4	0.7	0.8 - 1.9	0.4 - 1.4
K_{sec}	1.5	0.3	1.3 - 1.7	1.3 - 1.7
$\alpha^{Ge/Si}_{sec}$	3.4	1.0	2.9 - 4.0	3.3 - 8.4
K_{bio}	0.26	0.15	0.14 - 0.37	0.07 - 0.28
$\alpha^{Ge/Si}_{bio}$	0.62	0.28	0.35 - 0.83	0.30 - 0.79
$\Delta^{30}Si_{sec\text{-}diss}$ (‰)	−1.7	0.5	−2.10 - −1.39	−3.1 - −2.7
$\Delta^{30}Si_{bio\text{-}diss}$ (‰)	−1.0	0.5	−1.39 - −0.70	−2.3 - −2.0
$\Delta^{74}Ge_{sec\text{-}diss}$ (‰)	−2.3	0.2	−2.40 - −2.17	−2.7 - −2.5

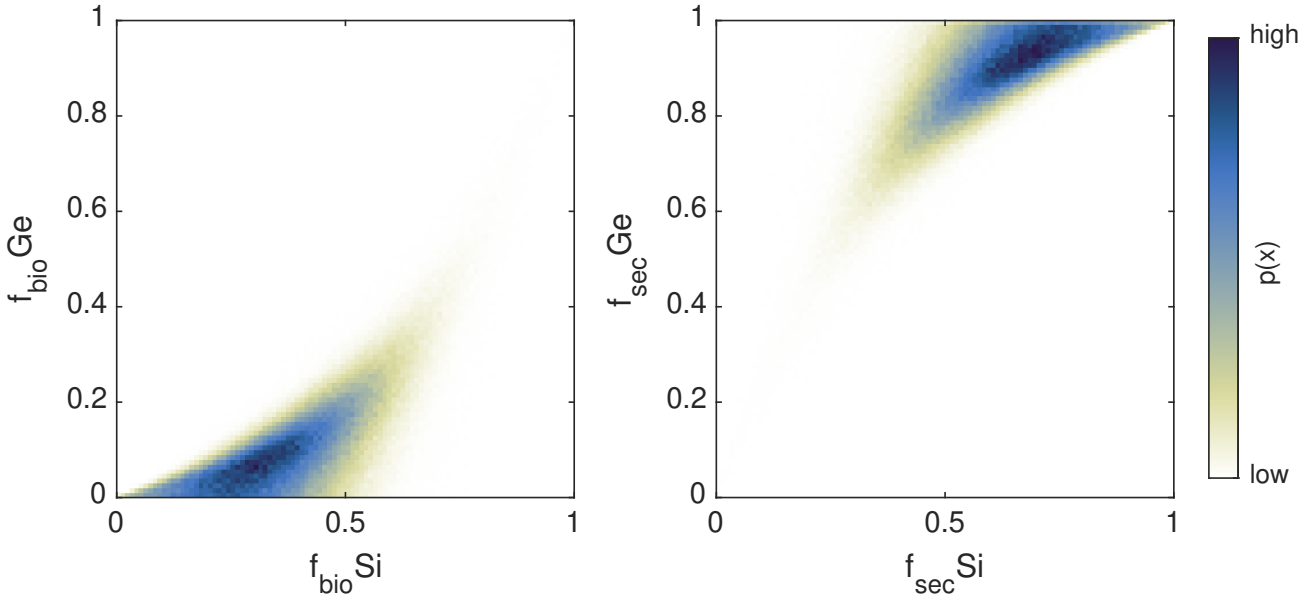

Figure S5. Isotopic mass balance model results for La Selva soils, showing the calculated Si and Ge partitioning between uptake via secondary mineral phases (sec) and vegetation (bio). Darker shade indicates higher probability density for the calculated values.

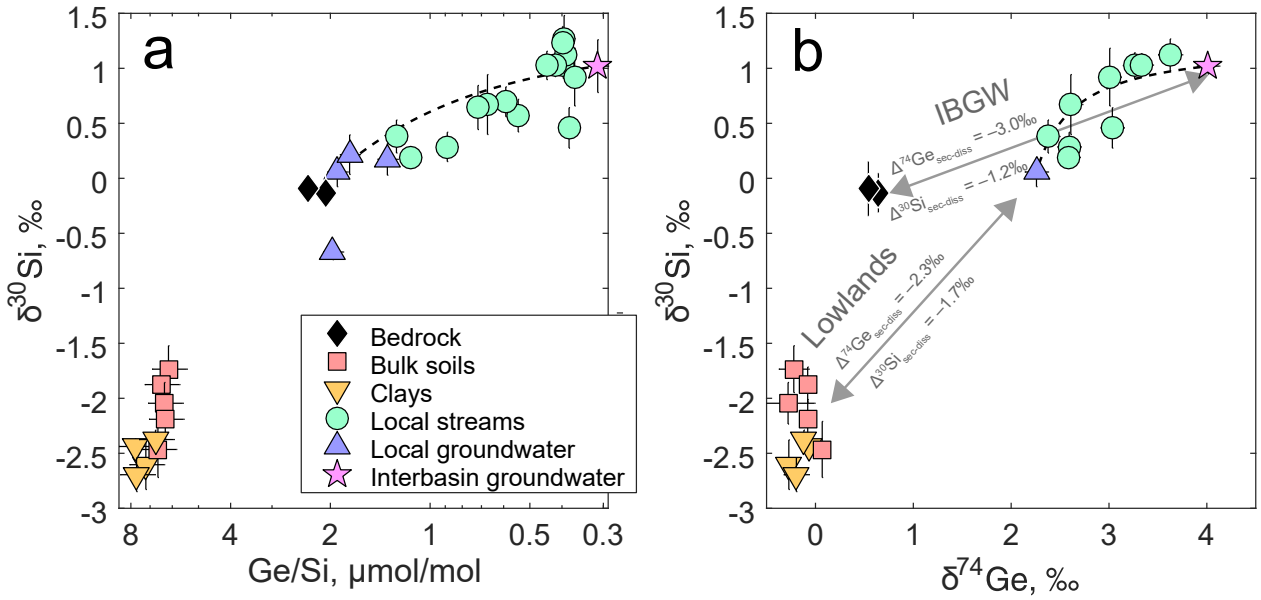

Figure S6. The relationship between Si isotopes and Ge/Si ratios (a) and Ge isotopes (b), in solids and fluids of La Selva. The dashed lines show an expected mixing relationship between lowland groundwater (sample LS03) and interbasin groundwater (sample CR05). The arrows in panel (b) show the determined fractionation factors for the two different weathering environments represented at this study site. Note the reversed direction and the log scale of Ge/Si axis in panel (a).